Neoplastic immune mimicry is a generalizable phenomenon in breast cancer and epithelial CD69 enables early tumor progression

Eric B. Berens[1,4*], Sokchea Khou[4], Elaine Huang[4], Amber Hoffman[4], Briana Johnson[4], Nell Kirchberger[4], Shamilene Sivagnanam[4], Nicholas L. Calistri[5], Daniel Derrick[5], Tiera A. Liby[5], Ian C. McLean[5], Aryn A. Alanizi[1], Furkan Ozmen[6,7], Tugba Y. Ozmen[6,7], Gordon B. Mills[6,7], E. Shelley Hwang[2], Pepper J. Schedin[4,7], Hugo Gonzalez[1,3], Zena Werb[1] (deceased), Laura M. Heiser[5,7], Lisa M. Coussens[4,7*]

[1]Department of Anatomy, University of California, San Francisco, CA, USA; [2]Department of Surgery, Duke University Medical Center, Durham, NC, USA; [3]Laboratory of Tumor Microenvironment and Metastasis, Centro Ciencia & Vida, Universidad San Sebastian, Santiago, Chile; [4]Departments of Cell, Developmental & Cancer Biology, [5]Biomedical Engineering, [6]Division of Oncological Sciences, and [7]Knight Cancer Institute, Oregon Health and Science University, Portland, OR, USA

***Corresponding Authors:** Eric B. Berens berense@ohsu.edu,
Lisa M. Coussens, coussenl@ohsu.edu

ABSTRACT

Dedifferentiation programs are commonly enacted during breast cancer progression to enable novel cellular phenotypes. Increased cellular plasticity within the neoplastic compartment of tumors correlates with disease aggressiveness, often culminating in greater resistance to cytotoxic therapies or the augmented ability to metastasize to distant organs. Here we report that subpopulations of dedifferentiated neoplastic breast epithelial cells express canonical leukocyte cell surface receptor proteins and have thus named this unique cellular program "immune mimicry." We document neoplastic cells engaging in immune mimicry within public human breast tumor single-cell RNA-seq datasets, histopathological breast tumor specimens, breast cancer cell lines, as well as in murine transgenic and cell line-derived mammary cancer models. Immune-mimicked neoplastic cells harbor hallmarks of dedifferentiation and appear enriched in treatment-resistant and high-grade breast tumors. We corroborated these observations in aggressive breast cancer cell lines where growth-arresting cytotoxic chemotherapies drove epithelial cells toward immune mimicry. Moreover, in subsequent proof-of-concept studies, we demonstrate that expression of the CD69 leukocyte activation marker by neoplastic cells confers a proliferative advantage that enhances early tumor growth. We conclude neoplastic breast epithelial cells that upregulate leukocyte surface receptors potentiate malignancy. Moving forward, neoplastic immune mimicry should be evaluated for prognostic utility in breast cancer to determine its stratification potential for patients with increased risks of tumor recurrence, metastasis, and therapeutic resistance.

INTRODUCTION

Tumors are complex ecosystems containing a variety of interacting cell types and cell states *(1)*. Research has sought to identify the cells driving tumor progression and this effort has led to both epithelial and stromal candidates *(2, 3)*. The search for these potentiators of malignancy has produced seminal discoveries including dedifferentiated tumor-initiating cells that fuel tumors despite existing in low abundance *(4)*. Aggressive tumors driven by these dedifferentiated subpopulations exhibit therapeutic resistance along with increased tumor recurrence and metastatic potential *(5, 6)*. The plasticity of dedifferentiated neoplastic cells renders them difficult to locate and eradicate, potentially contributing to cancer patient mortality *(7, 8)*. Unveiling the biomarkers and functions inherent in aggressive neoplastic could underlie more effective therapies; these are pressing tasks as the global burden of cancer continues to rise *(9)*.

Neoplastic cells that acquire stem-like characteristics often gain the ability to undergo metaplasia or mimic various stromal cell types *(10, 11)*. Studies have demonstrated that primary tumor growth and metastasis are fostered by neoplastic cells harboring transcriptional programs reminiscent of fibroblasts *(12)*, endothelia *(13)*, or even neurons *(14)*. The notion that neoplastic cells might also mimic leukocytes is suggested by recent research documenting unexpected expression of surface markers canonically attributed to leukocytes *(15–19)*. Highlights include aggressive breast carcinoma cells expressing the CD14 monocyte marker *(20)*, stem-like cutaneous squamous carcinoma cells expressing the CD80 B cell marker *(15)*, and pancreatic adenocarcinoma expressing the CD68 myelomonocytic marker *(16)*. There is even evidence that neoplastic epithelial cells upregulate the CD74 invariant chain of the MHC II molecule *(21)* or lymphocyte chemokine receptors, such as CXCR4 when disseminating *(22)*. Neoplastic cells can also acquire leukocyte CD45 via fusion with myeloid cells to generate circulating hybrids that promote metastasis *(19)*. In each of these instances, neoplastic cells appear to utilize canonical leukocyte surface receptors to enhance their intrinsic malignancy or to manipulate the stroma.

In this study, we identified subpopulations of dedifferentiated neoplastic epithelial cells expressing biological programs ascribed to endothelia, mesenchyme, neurons, or leukocytes in a single-cell RNA-sequencing (scRNA-seq) analysis of 70 human public breast tumors *(23, 24)*. We focused further on "immune mimicry" as an emergent phenomenon accompanying aggressive treatment-resistant disease. Immune-mimicked neoplastic cells upregulate variable combinations of >20 surface marker genes canonically expressed by leukocytes like CD3, CD14, CD18, CD45, CD68, CD69, CD74, and CD83, and were found in nearly every breast tumor. We endogenously corroborated this phenomenon in 12 human breast and murine mammary cancer cell lines, where cytotoxic therapy further induced immune mimicry in aggressive/metastatic lines. Neoplastic cells expressing the CD69 leukocyte activation marker *(25, 26)* were additionally validated in a cohort of 58 histopathological breast tumor specimens via multiplexed immunohistochemistry and we linked neoplastic CD69 to tumor growth in experimental breast cancer models. Together, our observations indicate that aggressive neoplastic breast epithelial cells express canonical leukocyte markers and the phenomenon appears widespread in breast cancer.

RESULTS

In silico identification of neoplastic immune mimicry in human breast tumors and reduction mammoplasties

The premise of our study was that neoplastic cells experiencing plasticity could be computationally

identified in breast cancer. We hypothesized that these neoplastic cell states, if detected, likely contribute to disease progression and are therefore present in different tumors. Our ensuing Seurat-based *(27)* scRNA-seq analysis leveraged human breast tumor datasets available in the public domain *(23, 24)*. We questioned whether stem-like neoplastic cells cluster with, or separately from, well-differentiated epithelium and thus developed a computational approach to detect them irrespective of their cluster location (**Fig. 1A**). This modified approach isolated neoplastic mammary epithelium by first removing multiplets *(28)*, thereafter collecting cells expressing cytokeratin biomarker genes (e.g. KRT14, KRT18, and KRT19) along with inferred copy number variations (CNVs) *(29)*. We carried out scRNA-seq preprocessing for 70 human breast tumors *(23, 24)* (**fig. S1A-G; fig. S2A-G; fig. S3A-G**) and 124 reduction mammoplasties *(30)* without CNV detection (**fig. S4A-F**) to generate merged datasets for downstream analyses.

Evaluating neoplastic epithelia from distinct breast tumors in the Pal *et al.* dataset *(23)* revealed distinct neoplastic scRNA-seq clusters mostly formed by cells from individual patients, presumably driven by interpatient variability (**Fig. 1B; fig. S5A-B**). We used Shannon-Weaver Diversity Index scoring to identify clusters comprised of neoplastic cells amongst different patients, reasoning such clusters could represent shared cell states. Six shared clusters had an elevated Shannon-Weaver Diversity Index along with evident enrichment of non-epithelial biological processes normally attributed to immune (myeloid or lymphoid), neural, mesenchymal, and endothelial cells (**Fig. 1C**; **fig. S5C-E**). Unexpected biological processes associated with these shared neoplastic clusters were largely corroborated in the other human breast tumor scRNA-seq datasets (**fig. S6A-E; fig. S7A-E)**. We were particularly intrigued by the possibility that neoplastic epithelia expressed genes ascribed to leukocytes and opted to investigate this phenomenon further. In doing so, we focused specifically on genes encoding cell surface receptors due to their potential clinical applicability as future biomarkers or therapeutic targets.

Upregulated within these shared neoplastic clusters were 23 surface receptor genes significantly associated with "myeloid-like" and/or "lymphoid-like" neoplastic cell phenotypes across the breast tumor scRNA-seq datasets (**Fig. 1D; fig. S5F; fig. S6F; fig. S7F**). Several genes notably encoded markers routinely used to distinguish leukocyte subsets: e.g. CD3, CD14, CD18, CD45, CD68, CD69, CD74, and CD83. Neoplastic cells expressing these were detected in the majority of breast tumors analyzed yet only as minority (<5%) subpopulations on average (**Fig. 1E**). We next evaluated neoplastic epithelial cells expressing the "myeloid-like" and "lymphoid-like" genes from all datasets and therein broadly refer to them as "immune-mimicked" going forward.

Immune-mimicked cells in human breast tumors exhibited significantly upregulated signatures indicative of mammary stem and progenitor cells *(31)*, the NFκB pathway, and proliferating leukocytes when compared to non-mimicked neoplastic epithelia (**Fig. 1G**; **fig. S5G; fig. S6G; fig. S7G**). We considered whether the NFκB pathway gnes might represent a conduit through which neoplastic cells activate immune surface receptor expression, given its dual roles in regulating immune responses as well as malignant cell behaviors *(32)*. These observations intersected with increased neoplastic immune mimicry in high-grade breast tumors (**Fig. G**). Importantly, we found evidence of immune mimicry in presumably non-neoplastic epithelial cells in reduction mammoplasties *(30)* suggesting that this state is not restricted to malignant epithelium (**fig. S8A-H**), thereby denoting the presence of immune mimicry in both homeostatic and diseased breast tissue.

Coexpression of multiple leukocyte surface receptors (**fig. S9A**) coincided with the upregulation of known breast tumor-initiation biomarkers (**fig. S9B**). Immune mimicry was more pronounced in breast tumors versus reduction mammoplasties (**fig. S9C**) with the greatest level of immune mimicry found in triple-negative breast cancer (TNBC) (**fig. S9D**). Comparing RNA expression for immune mimicry genes in neoplastic cells versus epithelia from reduction mammoplasties revealed a selective association of CD69 with malignant epithelia (**fig. S9E-F**). CD69 is a canonical leukocyte activation marker highly expressed on T cells where it enhances tissue retention and other functions including proliferation *(25, 26)*. We posited a parallel function for epithelial CD69 in cancer and selected this marker for follow-up studies.

Because CD69 is typically activated in leukocytes during inflammation and tissue stress *(25)*, we hypothesized that epithelial CD69 might arise in tissues subjected to cytotoxic therapy. We then compared breast tumors receiving cytotoxic therapy prior to resection versus those that were therapy-naïve. Our analysis revealed significantly elevated neoplastic CD69 expression after therapy (**Fig. 1H**) and in tumors containing fewer neoplastic cells (**Fig. 1I**). CD69-positive neoplastic cells in breast tumors were furthermore often classified as mitotic (**Fig. 1J**) based on cell cycle phase scoring performed in Seurat *(27)*. These observations engendered the possibility that neoplastic epithelia express CD69 amid cell stress to facilitate tumor growth.

To affirm the epithelial origin of immune-mimicked cells *in silico*, we verified that they reflected non-mimicked neoplastic epithelia concerning RNA features, RNA counts, mitochondrial reads, (**fig. S10A**) and doublet probability score (**fig. S10B**). Neoplastic cells expressing canonical leukocyte surface receptor genes were found outside and within immune-mimicked scRNA-seq clusters (**fig. S10C**). Hybrid cells within the immune-mimicked clusters ostensibly upregulated of leukocyte activation processes versus non-mimicked neoplastic cells (**fig. S10D**) while retaining aspects of epithelial differentiation versus leukocytes in general (**fig. S10E**). Lastly, we interrogated a ~2 million human peripheral blood mononuclear cell (PBMC) public dataset *(33)* in search of epithelial cells and discovered a tiny fraction expressing KRT18 though otherwise devoid of KRT14 and KRT19 (**fig. S10F-I**). Thus, the mammary cytokeratin profile of immune-mimicked cells was more closely related to non-mimicked neoplastic epithelia than PBMCs (**fig. S10I**). We next sought to validate our aforementioned scRNA-seq findings in additional settings, starting with the assessment of epithelial CD69 in a histopathological cohort of human breast tumor specimens.

Histopathologic confirmation of epithelial CD69 in human breast tumors

We hence evaluated expression of epithelial CD69 in 58 histopathological breast tumors via multiplexed immunohistochemistry which revealed minor subpopulations positive for both CD69 (yellow) and pan-cytokeratin (red) (**Fig. 2A-B**). See methods for more details. Here epithelial CD69 staining patterns ranged from heterogeneous and diffuse to concentrated depending on the histopathological region of cytokeratin-positive cells (**Fig. 2B**). To limit false-positives, we omitted CD69-low cells from contention and only considered CD69-high epithelium which led to positivity identified in over half of the cohort (**Fig. 2C**) with no statistical tropism for disease subtype (**fig. S11A-D**). There was a trend toward increased epithelial CD69 in tumors given cytotoxic therapy prior to resection (**fig. S11E**) where CD69-positive epithelial cells in these tumors also trended toward greater positivity for KI67 more frequently than CD69-neg cells (**fig. S11F-H**). Given the histopathological confirmation of epithelial CD69 expression, we

hypothesized that breast cancer cell lines would also express canonical leukocyte surface receptor genes and permit further functional examination of the relationship between CD69 and tumor behavior.

Neoplastic immune mimicry in breast and mammary cancer cell lines

The DepMap bulk RNA-seq database *(34)* was consequently probed for breast cancer cell line expression of immune mimicry surface genes detected via scRNA-seq (**Fig. 3A**). In these data, immune mimicry genes were significantly elevated in basal breast cancer cell lines compared to luminal or HER2-amplified subtypes (**Fig. 3B**) and significantly correlated with dedifferentiation and NFκB pathway activation signatures (**Fig. 3C-E**). We then experimentally validated a subset of the receptors as protein monostains in 10 human breast cancer cell lines using flow cytometry (FACS). Consistent with scRNA-seq analyses, these efforts unveiled minority subpopulations of viable cells expressing canonical immune surface receptors (e.g. CD3, CD14, CD18, CD45, CD69, CD74, CD83) that varied across biological replicates (**Fig. 3F-G**). Basal subtype cell lines exhibited greater average leukocyte receptor expression (**Fig. 3H; fig. S12A-B**) in agreement with DepMap RNA data (**Fig. 3A**). By flow cytometry, we discovered CD45-positive neoplastic cells were significantly smaller in size than CD45-negative cells (**Fig. 3I**), and additional co-staining revealed that CD45 often correlated with expression of other immune mimicry markers including CD52, CD69, CD74, and CD83 (**Fig. 3J**). Because CD45-positive cells were not enriched for tumor-initiation markers like CD44, CD133, KIT, or THY-1, we concluded that immune-mimicked cells likely represented novel subpopulations worthy of additional study (**fig. S12C**).

Neoplastic CD69 denotes a cell state capable of proliferating under harsh conditions

We hypothesized that leukocyte receptor positivity would increase in cell lines subjected to stress derived from cytotoxic therapy or serum starvation, based on observations for neoplastic CD69 in scRNA-seq and mIHC data (**Fig. 1H; fig. S11E**). Indeed, CD69 cell positivity increased in aggressive/metastatic cell lines like MDA-MB-231 and HCC 1806 following paclitaxel (**Fig. 4A; fig. S13A-C**). Using MDA-MB-231, we quantified leukocyte surface receptor expression in various additional cytotoxic stress conditions and uncovered consistently elevated positivity for CD45, CD69, and CD83 (**Fig. 4B**). Several proteins displayed an affinity for the manner of cell stress, exemplified by MDA-MB-231 CD3 upregulation in serum-free medium and in response to doxorubicin, but not in response to paclitaxel (**Fig. 4B**). Immune mimicry in less aggressive MCF-7 cells was not impacted by paclitaxel (**fig. S14C-D**), but induction of CD45 and CD69 in MDA-MB-231 after paclitaxel was witnessed at both RNA and protein levels indicating transcriptional activation or cell selection (**Fig. 4C**). Murine mammary 4T1 cells also had widespread expression of immune surface receptors following paclitaxel treatment (**fig. S14E-F**), with both CD69 RNA and protein being enhanced (**Fig. 4D**). Moreover, there was a correlation between cells expressing Ki67 and immune-mimicked cells expressing CD69 in untreated and paclitaxel-treated conditions for MDA-MB-231 (**Fig. 4F-G**) and 4T1 (**Fig. 4H-I**). Together, these data support the notion that neoplastic CD69 distinguishes a cell state capable of proliferating under harsh conditions.

Since harsh conditions are naturally elicited during tumor metastasis, we asked whether neoplastic CD45 and CD69 were increased on 4T1 and MDA-MB-231 in this context. Each cell line was transduced with an mCherry fluorescent tag to facilitate *in vivo* detection and then subjected to a tumor growth and metastasis assay in mice, followed by tissue collection and flow cytometry analyses (**fig. S15A**). At study endpoint, 4T1 mCherry cells were prospectively identified in single-

cell suspensions isolated from tumor, blood, and lung tissue via co-expression of mCherry with the CD24 and EPCAM epithelial markers (**fig. S15B-C**). Disseminated 4T1 cells in blood and lungs of BALB/c mice significantly upregulated CD45 expression, while CD69 was tropic for cells isolated from metastatic lungs (**fig. S15D**). Conducting a parallel study with MDA-MB-231 in immunocompromised NSG mice involved prospective retrieval using mCherry and CD44 (**fig. S15E-F**) where we observed MDA-MB-231 metastases in numerous organ sites that expressed human CD45 and CD69 (**fig. S15G**). Strikingly, in metastatic lungs, MDA-MB-231 CD69 declined as metastatic burden increased (**fig. S15H**) which raised the possibility that neoplastic cells might coopt CD69 for the early stages of metastatic outgrowth, akin to how leukocytes utilize CD69 for cell activation *(25, 26)*.

Experimental studies linking neoplastic CD69 to enhanced early tumor growth

To evaluate links between neoplastic CD69 and malignancy, we employed CRISPR-activation (CRISPR-a) to endogenously overexpress CD69 in MDA-MB-231 cells, hypothesizing this would enhance aggressive cell growth *in vitro* and *in vivo*. Activation of the doxycycline-induced CRISPR-a system led to prominent CD69 RNA and protein expression (**Fig. 5A-C**). MDA-MB-231 cells formed larger colonies during low-density expansion on soft-agar indicating enhanced growth *in vitro* (**Fig. 5D-E**). Orthotopic implantation of MDA-MB-231 cells into immunocompromised NSG mice and the subsequent activation of CD69 (**Fig. 5F**) notably accelerated early tumor growth with respect to the CRISPR-a control (**Fig. 5G-H; fig. S16A-C**), with the difference dissipating by study endpoint (**Fig. 5I-J; fig. S16D-F**). However, at endpoint, mice implanted with activated-CD69 MDA-MB-231 cells had significantly larger metastatic lung foci versus the control (**Fig. 5K-L**) despite no difference in overall number of lung lesions (**Fig. 5M**). These data implied that neoplastic CD69 was not likely impacting lung seeding, but instead the proliferative potential of early tumors and metastases.

We further investigated the impact of "high" versus "low" CD69 expression by utilizing magnetic bead sorting to compare proliferative potential of CD69-high vs CD69-low subpopulations in MDA-MB-231 and 4T1 (**Fig. 6A**). Endogenous retrieval of CD69-high fractions was highly inefficient due to the small subpopulation sizes in routine culture conditions and thus required sorting of hundreds of millions of cells per replicate. CD69-high MDA-MB-231 cells exhibited RNA enrichment for both CD69 and NFKB1 (**Fig. 6B-C**), showed enrichment trends for other NFκB pathway genes (**fig. S17A-E**), and had improved growth kinetics when plated at low density *in vitro* (**Fig. 6D**). Magnetically-sorted CD69-high 4T1 cells were similarly enriched for CD69 and NFKB1 RNA expression (**Fig. 6E-F**) along with other NFκB pathway genes (**fig. S17F-J**). We orthotopically implanted CD69-high and CD69-low 4T1 cells at low density into syngeneic BALB/c mice where CD69-high cells more efficiently formed tumors (**Fig. 6G-H**), with unenriched cells representing the median of these two conditions (**fig. S17K-P**). Magnetic sorting and CRISPR-a experiments therefore jointly established that neoplastic CD69 impacts early tumor growth.

We subsequently conducted loss-of-function studies to determine the extent to which neoplastic CD69 governed early tumor growth and hypothesized its absence would be detrimental. These experiments were conducted in MMTV-PyMT-chOVA mice *(35)* to assess how loss of epithelial CD69 impacted the kinetics of tumor progression. Before initiating these studies, we confirmed that MMTV-PyMT-chOVA tumor cells contained a CD69-positive subpopulation (**Fig. 7A**)

expressing higher levels of Ki67 (**Fig. 7B**), and then we intercrossed MMTV-PyMT-chOVA mice with mice harboring a homozygous deletion of CD69 *(36, 37)* (**Fig. 7C**). Tumor incidence in PyMT-CD69$^{KO/KO}$ mice was not significantly altered from the PyMT-CD69$^{KO/+}$ control (**fig. S18A-C**), however, early tumor growth was significantly impeded in PyMT-CD69$^{KO/KO}$ mice where individual tumors exhibited a significantly increased doubling time (**Fig. 7D-G**). As such, total tumor burden in PyMT-CD69$^{KO/KO}$ mice was decreased (**Fig. 7H)** despite on average developing similar numbers of tumors as the PyMT-CD69$^{KO/+}$ control (**fig. S18D**).

We hypothesized that differences in host-derived CD69 could underlie some of the *in vivo* tumor growth phenotype, so we dissociated PyMT-CD69$^{KO/+}$ and PyMT-CD69$^{KO/KO}$ tumor cells and injected them back into syngeneic CD69-proficient (CD69$^{KO/+}$) control mice (**Fig. 7I**). We selected three pairs of tumors for this experiment that arose in equivalent mammary glands and reached similar endpoint sizes (**fig. S18E-G**). The attenuated ability of dissociated PyMT-CD69$^{KO/KO}$ cells to reestablish tumors in CD69$^{KO/+}$ recipients demonstrated retention of their original phenotype (**Fig. 7J-K**) and recapitulated observations using magnetically-sorted 4T1 cells (**Fig. 6H**). Additional support for CD69 intrinsically regulating neoplastic growth was provided by CRISPR/Cas9 experiments with MDA-MB-231 cells (**fig. S18A**), where CD69 disruption prevented CD69 induction and attenuated cell growth *in vitro* (**fig. S18B-C**). The ultimate conclusion of our study was that neoplastic breast cancer cells expressed leukocyte surface receptors and neoplastic CD69, in particular, potentiates malignant growth under harsh conditions *in vitro* and *in vivo*.

DISCUSSION

Our study uncovered pervasive neoplastic immune mimicry in human breast tumors and related cell lines. In public human breast tumor scRNA-seq datasets, a minority subpopulation of neoplastic epithelial cells expressed combinations of 23 surface receptor genes typically attributed to leukocytes including CD3, CD14, CD18, CD45, CD68, CD69, CD74, and CD83. Neoplastic cells engaging in immune mimicry concomitantly upregulated dedifferentiation programs, NFκB pathway and proliferative signatures. Additionally, we detected rare subpopulations of presumed non-malignant epithelia expressing leukocyte surface receptors in reduction mammoplasties. *In silico*, neoplastic CD69 was elevated in breast tumors versus reduction mammoplasties, especially those treated with neoadjuvant cytotoxic therapy and coexpressed in cells with a mitotic phenotype. We subsequently validated epithelial CD69 in a histopathological cohort of 58 humor breast tumors by multiplexed IHC. Our research also revealed consistent, albeit small, subpopulations expressing canonical immune surface receptors in breast and mammary cancer cell lines. Neoplastic immune mimicry was further induced in aggressive/metastatic cell lines subjected to cytotoxic chemotherapy, exemplified by MDA-MB-231 and 4T1. CD69-positive MDA-MB-231 and 4T1 cells were additionally enriched for Ki67 and potentiated early tumor growth upon implantation into mice. Finally, homozygous deletion of CD69 in MMTV-PyMT-chOVA mice conversely hindered mammary tumor growth.

In leukocyte biology, CD69 is a prominent indicator of early cell activation with multiple functions like facilitating tissue retention and cell metabolism *(25, 26)*. An early-activation marker like CD69 is challenging to study due to its dynamic regulation in cells; a fact woven throughout our efforts to discern its functional relevance in breast cancer but worthy of investigating due it potentially representing an early biomarker for patient stratification. This concept is highlighted

by our observation that neoplastic CD69 is associated with increased cell proliferation, especially amid harsh conditions like cytotoxic chemotherapy or in distal metastases. Recently, others have reported a role for epithelial CD69 in ovarian cancer that emerges under hypoxia *(38)*, indicating yet another route for CD69 induction. Harnessing antibodies to deliver innovative therapies to CD69-positive neoplastic cells could provide a novel strategy for overcoming drug resistance in a subpopulation that eludes growth control.

Although we sought to document convincing evidence for neoplastic immune mimicry in breast tumors and cell lines, we recognize that additional research is required to unveil the true extent of this phenomenon. A next step might entail probing DNA within cells expressing canonical leukocyte receptors to determine whether expression of the receptors is associated with specific breast cancer mutations. Lineage-tracing or barcoding experiments, especially those conducted *in vivo*, could also help demonstrate the neoplastic origin of immune-mimicked cells and the degree of plasticity in expression of immune markers. Pinpointing transcriptional regulators including the NFκB pathway that might elicit leukocyte gene expression in neoplastic cells would likewise be informative, as would studies determining if the function of receptors in neoplastic cells reflect known roles in leukocytes. Because leukocyte gene expression in structural cells outside the immune system could modulate immune-epithelial interactions *(39)*, future research should hence address whether immune-mimicked cells can evade anti-tumoral immunity as described for neoplastic cells expressing leukocyte surface receptors in other cancer lineages *(15–17)*.

Neoplastic cells generally expressing leukocyte surface receptors would have ramifications for the detection and treatment of breast cancer. For example, we have previously reported that leukocytes readily infiltrate breast tumors following cytotoxic therapy *(40, 41)*, yet here we also establish that neoplastic epithelia express immune markers including CD45 and CD69 in similar conditions. It is therefore possible that immune mimicry leads to neoplastic cells avoiding clinical detection after therapy, due to our current reliance on surface features when discerning cell types. In this same vein, it has been reported that circulating tumor cells bound to CD45-positive cells described as leukocytes more effectively grow as distant metastases *(42, 43)*. In light of our research, it is possible that some of these assumed "leukocytes" could be neoplastic cells endogenously expressing CD45 when transiting through the body, a fact that, if confirmed, could inspire new ways to detect micrometastases. These findings thematically intersect with previous work identifying CD45-positive neoplastic-immune hybrids in the blood of patients afflicted with uveal melanoma *(19)* and additional biomarkers affiliated with these cells *(44)*. Since our flow cytometry analyses uncovered that neoplastic breast cells endogenously positive for CD45 are significantly smaller than the CD45-negative variety, we would caution against trusting small cell size as a distinguishing feature for leukocytes. Additional research in areas like these will be required before neoplastic immune mimicry can be clinically translated.

Computational biologists have questioned the utility of 2D embeddings to capture biological complexity during scRNA-seq analysis *(45)* and our study demonstrates that it is sometimes worth thinking beyond cluster location when inferring cell types. Our method of initially gating breast epithelia via marker expression in lieu of cluster location exposed provocative dedifferentiated/mimicked neoplastic cell states: developmental mimicry, endothelial mimicry, immune mimicry, mesenchymal mimicry, and neuronal mimicry. Although here we pursued neoplastic immune mimicry, the repertoire of genes that constitute each of these cell states and

their roles in other cancer lineages deserves greater attention. Future studies might also consider if neoplastic cells engaging in these phenotypes could concomitantly lack mammary cytokeratins after, for example, an epithelial-mesenchymal transition *(12)*. In the era of single-cell technologies, it is incumbent upon investigators to acknowledge and evaluate cell plasticity when conducting analyses.

MATERIALS AND METHODS

scRNA-seq analysis

Count matrices for human breast tumor scRNA-seq datasets *(23, 24)* were downloaded from GEO (GSE161529, GSE176078) and supplemented with additional tumors from the PANNTHR trial at the Oregon Health & Science University. All scRNA-seq analyses were conducted in R using Seurat-V5 *(27)*. Tumor samples containing all cells were first processed separately and subjected to filtering for nfeatures (lower limit >200; upper limit tailored per sample) and mitochondrial reads (<10% for Pal *et al.* and PANNTHR (NCT04481113) datasets, < 20% for Wu *et al.* dataset). DoubletFinder *(28)* was then applied to each sample to identify and remove multiplets, assuming a ~5% multiplet rate per ~10,000 cells. Singlet cells were next collected for downstream analysis after which epithelia were extracted using a gating threshold > 1 for KRT14, KRT18, or KRT19. Epithelial cells were extracted from the Kumar *et al.* reduction mammoplasty dataset *(30)* in the manner described above. InferCNV *(29)* was subsequently performed on individual tumor samples to identify neoplastic epithelium by comparison to an epithelial reference. This reference was built by combining 100 epithelial cells downsampled from the 124 reduction mammoplasties in which we ascertained 8 reference groups. We considered tumor epithelial cells to be neoplastic if chromosomal CNVs were inferred versus these 8 reference groups.

After identifying neoplastic epithelia in each tumor sample, or mammary epithelia in the reduction mammoplasties, we next merged scRNA-seq samples within datasets. Our decision to merge (i.e. not integrate) samples without regressing cell cycle status was predicated on a desire to maintain interpatient heterogeneity. Diverse scRNA-seq clusters were identified using Shannon Weaver Diversity Index scoring via the vegan R package *(46)* and clusters were considered diverse if this score was above 1.5. Neoplastic (or epithelial) cells were defined as immune-mimicked if they resided within an immune-like scRNA-seq cluster. Genes significantly upregulated in diverse clusters were subjected to FGSEA *(47)* to identify significantly enriched biological processes. Surface receptors attributed to myeloid-like and lymphoid-like phenotypes involved filtering differentially enriched genes with a list of human cluster of differentiation (CD) surface markers from UniProt (release: 2024_06). CD receptors were only considered if they showed a fold-change increase of >1.5 and $p < 0.001$ in immune-mimicked scRNA-seq clusters.

Many scRNA-seq plots presented in the manuscript were generated by quantifying either the percent of neoplastic/epithelial cells engaging in immune mimicry or the percent of cells expressing a given receptor. These positivity comparisons were done to facilitate drawing parallels between scRNA-seq and FACS analyses. Although sample merging was done at the dataset level during scRNA-seq analysis, all samples were combined when making plots with extracted expression matrices, linked metadata, and clinical attributes. Signatures used for comparing immune-mimicked and non-mimicked cells were obtained from MSigDB *(48)*, the cell cycle analysis followed the Seurat tool's vignette, and the correlation plot was generated with R's corrplot package *(49)*. Last, the human PBMC dataset used for scRNA-seq analysis was accessed

via the portal accompanying its publication *(33)*.

Multiplexed immunohistochemistry

Primary breast tumor tissue was acquired from two sources for our histopathological evaluation of epithelial CD69. These sources encompassed a breast tumor tissue microarray created from 26 patient specimens retrospectively banked at the Oregon Health & Science University, which we then supplemented with 32 other breast tumor tissues from a previous cohort *(50)*. FFPE tissue sections of ~5 μm thickness from this pooled cohort of 58 primary breast tumors were then subjected to mIHC as previously described *(51)*. The antibodies we used are found in Table S1 and, notably, the CD69 antibody was specifically chosen due to its widespread use in The Human Protein Atlas. To detect surface receptor protein expression via mIHC analysis, we first created a nuclei mask from the H3NUCA stain and then expanded segmented nuclei using a propagation algorithm based on PanCK staining. Each cell's segmentation was expanded if it had PanCK stain while neighboring cells maintained their original nuclei segmentation. Epithelial CD69 was distinguished in the Image Cytometry software version of FCS Express with the following cellular gates: PanCK-pos, CD45-neg, and CD69-high. We used a conservative gating strategy when enumerating epithelial CD69 positivity in breast tumors to reduce possible false positives. When generating pseudocolored composite images, we assigned markers the following colors: H3NUCA (blue), CD3 (cyan), CD45 (magenta), CD69 (yellow), PANCK (red), VIM (green). Epithelial CD69 is visually portrayed as overlapping yellow and red colors.

Cell line studies

In silico evaluation of leukocyte surface receptor expression in human breast cancer cell lines leveraged public RNA-seq data downloaded from the DepMap project *(34)* (https://depmap.org/portal). All cell lines experimentally used in this study were obtained from the American Type Culture Collection. The exception is the PyMT-chOVA cell line originated in the Max Krummel Lab and was acquired from the Zena Werb Lab at UCSF. The following cell lines were maintained in DMEM + 10% FBS: 4T1, CAMA-1, JIMT-1, MCF-7, MDA-MB-231, MDA-MB-468, PyMT-chOVA, and SK-BR-3. The following lines were maintained in RPMI 1640 + 10% FBS: BT-474, HCC 1806, T-47D, and ZR-75-1. Cell culture medium source: DMEM (Fisher, cat #11-995-073), RPMI (Fisher, cat #11-875-093), FBS (ThermoFisher Scientific, cat. #10438026). Each cell line was propagated under subconfluent conditions and dissociated with trypsin-EDTA (0.25%) (Fisher, cat. #25-200-114) for all assays.

Drug treatments on cell lines involved paclitaxel (Sigma-Aldrich, cat. #T7402) or doxorubicin (Selleck Chemicals, cat. #S1208) solubilized in DMSO. Human breast cancer cell lines were treated with 80 nM paclitaxel or 100 nM doxorubicin, and murine mammary cancer cell lines were subjected to 200 nM paclitaxel. These concentrations aimed to achieve a half-maximal inhibitory concentration (IC50) on cell growth. All treatments were initiated 24 hours after low-density cell plating and persisted for 72 hours. Irradiation (8 Gy) and serum-free medium treatments followed this same paradigm, which began also 24 hours after plating. All cell line morphology photographs were acquired on a Nikon Eclipse Ts2R microscope in either untreated conditions or at treatment endpoint.

Cell growth was assessed via soft-agar and crystal violet assays. Evaluating colony formation *in vitro* involved plating MDA-MB-231 cells at low density and within 0.3% agar onto a 0.5% layer

of agar. Half-medium exchanges were performed every 5 days for one month, after which colonies were stained with 0.005% crystal violet. Images were acquired on a dissection microscope and binarized in Fiji (ImageJ), after which colony size per well was calculated as pixel area. For general cell proliferation assays, cell growth was quantified in a 96-well vessel after crystal violet staining (0.1%), where 50 cells per well represented a sparse plating density and 500 cells per well was standard.

Flow cytometric assessment of immune mimicry

All cell lines were dissociated with trypsin-EDTA (0.25%) (Fisher, cat. #25-200-114) for flow cytometry (FACS). FACS staining was done as monostains or all stains where indicated, and data were acquired on a 5-laser Cytek Aurora Spectral Flow Cytometer on cells fixed with BD Cytofix (BD, cat. #554655). The antibodies used in this study are listed in Table S2 (human) and Table S3 (murine). KI67 staining was performed on cells following fixation/permeabilization (ThermoFisher Scientific, cat. #88-8824-00). We included mouse-CD45-PerCP when conducting FACS on digested organs containing mCherry-pos MDA-MB-231. FACS done on CD69 CRISPR-a MDA-MB-231 cells necessitated changing marker fluorophores to accommodate high eGFP levels in the cell line; we used Zombie Violet and CD69-APC and ran these samples on a BD LSRFortessa. FACS data were analyzed in FCS Express, where we applied upstream gates to exclude cellular doublets, dead cells, and high autofluorescence. The FACS marker correlation plot was made with the corrplot R package *(49)* and tSNE plots were generated with the Spectre R package *(52)*.

qRT-PCR assessment of immune mimicry

The qRT-PCR primers used in this study are shown in Table S4. RNA extractions were performed with an RNeasy kit (Qiagen, cat. #74104) and cDNA was synthesized using either SuperScript VILO Master Mix (ThermoFisher Scientific, cat. #11-755-050) or iScript (Bio-Rad, cat. #1708891). Quantitative PCR was conducted on an Applied Biosciences ViiA 7 with PowerUp SYBR Green (ThermoFisher Scientific, cat. #A25741) or on a BioRad Opus with iTaq Universal SYBR Green (Bio-Rad, cat. #1725121). Gene expression in cell lines was normalized to either ACTB or GAPDH. CD69 expression after CRISPR/Cas9 editing was evaluated with primers binding upstream of the sgRNA target sites. All primer oligos were purchased from Integrated DNA Technologies.

CRISPR editing

All sgRNA sequences used to overexpress or disrupt CD69 are found in Table S5. All CD69 sgRNA oligos were identified in the CHOPCHOP database (https://chopchop.cbu.uib.no/) and obtained from Integrated DNA Technologies. CD69 sgRNAs were cloned using the annealed oligo method into their requisite vector backbones. Endogenously overexpressing CD69 employed the CRISPR Synergistic Activation Mediator system. MDA-MB-231 cells were stably transduced with the following plasmids for CRISPR-activation experiments: pHAGE TRE dCas9-VP64, (AddGene plasmid #50916), lenti sgRNA(MS2)_Puro backbone (AddGene plasmid #73795), LentiMPH v2 (AddGene plasmid #89308), and pLV-eGFP (AddGene plasmid #36083) *(53–56)*. MDA-MB-231 cells were treated with 1μg/ml doxycycline to induce CD69 during CRISPR-activation experiments. MDA-MB-231 cells were stably transduced with lentiCRISPR v2 (AddGene plasmid #52961) for CD69 CRISPR/Cas9 disruption studies *(55)*.

Magnetic cell sorting

CD69-high neoplastic cells were sorted from MDA-MB-231 and 4T1 cultures using an EasySep PE Positive Selection Kit II (STEMCELL Technologies, cat. #17684). We used human-CD69-PE (BioLegend cat. #310905) and mouse-CD69-PE (BioLegend cat. #104512) antibodies for these experiments. Each sorting replicate was conducted on cultured cells grown under standard conditions for 72h hours to a final confluency of ~75%. Sorting 200 million cells per replicate, on average, yielded around 50,000 CD69-high cells and thereby limited downstream applications.

Orthotopic *in vivo* tumor studies

Orthotopic tumor growth was evaluated in all cell lines implanted into the 4th left mammary gland of female mice between 6-8 weeks of age. Female NSG mice (Jackson Laboratory, cat. #005557) received 1 million MDA-MB-231 cells suspended in DMEM containing 50% Matrigel GFR Basement Membrane Mix (Corning, cat. #354230). Mice used for CD69 CRISPR-a experiments were fed a 200 mg/kg doxycycline diet (Bio-Serv cat. #S3888) that was initiated 8 days after MDA-MB-231 implantation. Metastases were analyzed in H&E lung sections using QuPath to quantify the size of individual lesions and the number of cells within them. Orthotopic experiments with 4T1 cells sorted on CD69 involved implanting 1,000 cells orthotopically into BALB/c mice (Charles River, cat. #028) in PBS. In some instances, a mCherry fluorescent tag (AddGene plasmid #36084) was stably transduced into 4T1 and MDA-MB-231 cells to facilitate their retrieval from tissue *in vivo*. In these studies, we implanted 200,000 4T1 cells in PBS into BALB/c mice or 1 million MDA-MB-231 cells in Matrigel GFR into NSG mice. For orthotopic reinjection experiments with dissociated MMTV-PyMT-chOVA-CD69$^{KO/+}$ or -CD69$^{KO/KO}$ tumors, we first selected tumors from each background that: developed in the same mammary gland, grew at similar rates, and reached a similar size at endpoint. We found three pairs of tumors that we reinjected into CD69$^{KO/+}$ mice lacking the PyMT transgene. When required, mammary tumors were digested in DMEM containing 2 mg/ml Collagenase A (Roche cat. #11088793001) and 50 U/ml DNase I (Roche cat. #10104159001) with agitation for 30 min at 37°C. Experiments attained endpoint when tumors reached 2 cm in diameter, if they became ulcerated, or if mice exhibited outward signs of suffering.

Genetically engineered *in vivo* tumor studies

Spontaneous mammary tumor growth was assessed in MMTV-PyMT-chOVA-CD69$^{KO/KO}$ mice that were generated by crossing MMTV-PyMT-chOVA mice *(35)* with CD69$^{KO/KO}$ mice *(36, 37)*. Knockout of the CD69 gene was confirmed through genotyping. Mice were monitored for mammary tumors starting at 100 days, and at 3/4-day intervals thereafter until endpoint. We recorded tumor incidence and size data that were compared between MMTV-PyMT-chOVA-CD69$^{KO/+}$ and -CD69$^{KO/KO}$ mice. Tumor growth was evaluated between these groups and doubling time was calculated from an exponential regression model, tumor slope from a linear regression model, and both were subjected to outlier removal in GraphPad. Tumor burden per mouse was calculated by summing all of its tumors, and we subjected these data to nonlinear regression (Gompertz growth) to calculate when tumor burden crossed the 1000 mm^3 threshold. For all MMTV-PyMT experiments, mice were euthanized when tumors reached 2 cm in diameter, if the tumors became ulcerated, or if mice showed visible signs of suffering.

Statistical analyses

Statistical analyses were carried out with GraphPad Prism v10. We considered the distribution of

data points when conducting statistics and the tests used in this study include: analysis of variance, linear regression, nonlinear regression, Pearson correlation, Spearman correlation, Mann-Whitney test, Wilcoxon signed-rank test, and Student's t-test. All experimental data points are shown as biological replicates.

Acknowledgments
The authors acknowledge members of the Werb, Heiser and Coussens laboratories for critical feedback and insight, as well as the OHSU Shared Resources and NIH/NCI P30 CA069533. We also acknowledge the OHSU Knight Cancer Institute SMMART clinical trials program for technical assistance and research contributions to the PANNTHR study supported by GSK (NCT04481113) and Eli Lilly and Company, who reviewed preliminary version of the manuscript prior to submission. This research was further enabled by the following funding sources: NIH/NCI K00 CA212132 and the Collins Medical Trust to E.B.B.; NIH/NCI T32 CA254888 to E.B.B. and N.L.C.; Jayne Koskinas Ted Giovanis Foundation for Health and Policy, Kuni Foundation and NIH research grant U54-CA209988 to L.M.H.; the Susan G Komen Foundation and the National Foundation for Cancer Research to L.M.C. Dr. Steve Jameson generously provided the CD69$^{KO/KO}$ mice and illustrations were created with BioRender.com. The authors are solely responsible for the final content and interpretation. The Jayne Koskinas Ted Giovanis Foundation for Health and Policy is a private foundation committed to critical funding of cancer research. The opinions, findings, conclusions or recommendations expressed in this material are those of the author(s) and not necessarily those of the Jayne Koskinas Ted Giovanis Foundation for Health and Policy or its respective directors, officers, or staff.

Author Contributions
Conceptualization, E.B.B., Z.W., L.M.C., L.M.H. Computational analysis, E.B.B. Computational insights, L.M.H., H.G., N.L.C., D.D., T.A.L., I.C.M. Conducted *in vitro* experiments, E.B.B., S.K., A.H., B.J. Conducted *in vivo* experiments, E.B.B., S.K., E.H. Results Interpretation, E.B.B., S.K., E.H., A.H., B.J., N.L.C., D.D., T.A.L., I.C.M., H.G., L.M.H., L.M.C. Generated PANNTHR scRNA-seq data, F.O., T.Y.O., G.B.M. Plasmid cloning, E.B.B., A.A.A. Histopathological sample acquisition, E.S.K. Histopathological TMA design, P.S., L.M.C., E.B.B. Multiplexed immunohistochemistry analysis, E.B.B., N.K., S.S. Wrote the manuscript, E.B.B. Edited the manuscript, L.M.C., L.M.H., G.B.M. Supervision, Z.W., L.M.C., L.M.H.

Competing Interests
L.M.C. has received reagent support from Cell Signaling Technologies, Syndax Pharmaceuticals, Inc., ZielBio, Inc., and Hibercell, Inc.; holds sponsored research agreements with Prospect Creek Foundation, grant support from Susan G. Komen Foundation, National Foundation for Cancer Research, and the National Cancer Institute; is on the Advisory Board for Carisma Therapeutics, Inc., CytomX Therapeutics, Inc., Kineta, Inc., Hibercell, Inc., Cell Signaling Technologies, Inc., Alkermes, Inc., NextCure, Guardian Bio, Dispatch Biotherapeutics, AstraZeneca Partner of Choice Network (OHSU Site Leader), Genenta Sciences, Pio Therapeutics Pty Ltd., and Lustgarten Foundation for Pancreatic Cancer Research Therapeutics Working Group. G.B.M. has received support from AstraZeneca, Zentalis, and Nanostring; is on the advisory board for Amphista, Astex, AstraZeneca, BlueDot, Ellipses Pharmaceuticals, ImmunoMET, Leapfrog Bio, Bruker/Nanostring, Neophore, Nerviano, Nuvectis, Pangea, PDX Pharmaceuticals, Qureator, Rybodyne, Signalchem Lifesciences, Tarveda, Turbine, and Zentalis Pharmaceuticals; has a

financial stake in Bluedot, Catena Pharmaceuticals, ImmunoMet, Nuvectis, RyboDyne, SignalChem Lifesciences, Tarveda, and Turbine.

REFERENCES

1. K. E. de Visser, J. A. Joyce, The evolving tumor microenvironment: From cancer initiation to metastatic outgrowth. *Cancer Cell* **41**, 374–403 (2023).

2. G. M. Wahl, B. T. Spike, Cell state plasticity, stem cells, EMT, and the generation of intra-tumoral heterogeneity. *NPJ Breast Cancer* **3**, 14 (2017).

3. K. M. Bussard, L. Mutkus, K. Stumpf, C. Gomez-Manzano, F. C. Marini, Tumor-associated stromal cells as key contributors to the tumor microenvironment. *Breast Cancer Res.* **18**, 84 (2016).

4. K. Ishizawa, Z. A. Rasheed, R. Karisch, Q. Wang, J. Kowalski, E. Susky, K. Pereira, C. Karamboulas, N. Moghal, N. V. Rajeshkumar, M. Hidalgo, M. Tsao, L. Ailles, T. K. Waddell, A. Maitra, B. G. Neel, W. Matsui, Tumor-Initiating Cells Are Rare in Many Human Tumors. *Cell Stem Cell* **7**, 279–282 (2010).

5. E. Charafe-Jauffret, C. Ginestier, F. Iovino, J. Wicinski, N. Cervera, P. Finetti, M.-H. Hur, M. E. Diebel, F. Monville, J. Dutcher, M. Brown, P. Viens, L. Xerri, F. Bertucci, G. Stassi, G. Dontu, D. Birnbaum, M. S. Wicha, Breast Cancer Cell Lines Contain Functional Cancer Stem Cells with Metastatic Capacity and a Distinct Molecular Signature. *Cancer Res.* **69**, 1302–1313 (2009).

6. S. Liu, M. S. Wicha, Targeting Breast Cancer Stem Cells. *J. Clin. Oncol.* **28**, 4006–4012 (2010).

7. S. Yuan, R. J. Norgard, B. Z. Stanger, Cellular Plasticity in Cancer. *Cancer Discov.* **9**, 837–851 (2019).

8. A. Pérez-González, K. Bévant, C. Blanpain, Cancer cell plasticity during tumor progression, metastasis and response to therapy. *Nat. Cancer* **4**, 1063–1082 (2023).

9. H. M. Bizuayehu, K. Y. Ahmed, G. D. Kibret, A. F. Dadi, S. A. Belachew, T. Bagade, T. K. Tegegne, R. L. Venchiarutti, K. T. Kibret, A. H. Hailegebireal, Y. Assefa, M. N. Khan, A. Abajobir, K. A. Alene, Z. Mengesha, D. Erku, D. A. Enquobahrie, T. Z. Minas, E. Misgan, A. G. Ross, Global Disparities of Cancer and Its Projected Burden in 2050. *JAMA Netw. Open* **7**, e2443198 (2024).

10. T. P. Reddy, R. R. Rosato, X. Li, S. Moulder, H. Piwnica-Worms, J. C. Chang, A comprehensive overview of metaplastic breast cancer: clinical features and molecular aberrations. *Breast Cancer Res.* **22**, 121 (2020).

11. P. E. Saw, Q. Liu, P.-P. Wong, E. Song, Cancer stem cell mimicry for immune evasion and therapeutic resistance. *Cell Stem Cell* **31**, 1101–1112 (2024).

12. A. Dongre, R. A. Weinberg, New insights into the mechanisms of epithelial–mesenchymal transition and implications for cancer. *Nat. Rev. Mol. Cell Biol.* **20**, 69–84 (2019).

13. E. Wagenblast, M. Soto, S. Gutiérrez-Ángel, C. A. Hartl, A. L. Gable, A. R. Maceli, N. Erard, A. M. Williams, S. Y. Kim, S. Dickopf, J. C. Harrell, A. D. Smith, C. M. Perou, J. E. Wilkinson, G. J. Hannon, S. R. V. Knott, A model of breast cancer heterogeneity reveals vascular mimicry as a driver of metastasis. *Nature* **520**, 358–362 (2015).

14. A. E. Whiteley, D. Ma, L. Wang, S.-Y. Yu, C. Yin, T. T. Price, B. G. Simon, K. R. Xu, K. A. Marsh, M. L. Brockman, T. M. Prioleau, K. I. Zhou, X. Cui, P. E. Fecci, W. R. Jeck, C. M. McCall, J. L. Neff, D. A. Sipkins, Breast cancer exploits neural signaling pathways for bone-to-meninges metastasis. *Science* **384**, eadh5548 (2024).

15. Y. Miao, H. Yang, J. Levorse, S. Yuan, L. Polak, M. Sribour, B. Singh, M. D. Rosenblum, E. Fuchs, Adaptive Immune Resistance Emerges from Tumor-Initiating Stem Cells. *Cell* **177**, 1172-1186.e14 (2019).

16. R. Ajina, Z. X. Malchiodi, A. A. Fitzgerald, A. Zuo, S. Wang, M. Moussa, C. J. Cooper, Y. Shen, Q. R. Johnson, J. M. Parks, J. C. Smith, M. Catalfamo, E. J. Fertig, S. A. Jablonski, L. M. Weiner, Antitumor T-cell Immunity Contributes to Pancreatic Cancer Immune Resistance. *Cancer Immunol Res.* **9**, 386–400 (2021).

17. E. Gangoso, B. Southgate, L. Bradley, S. Rus, F. Galvez-Cancino, N. McGivern, E. Güç, C.-A. Kapourani, A. Byron, K. M. Ferguson, N. Alfazema, G. Morrison, V. Grant, C. Blin, I. Sou, M. A. Marques-Torrejon, L. Conde, S. Parrinello, J. Herrero, S. Beck, S. Brandner, P. M. Brennan, P. Bertone, J. W. Pollard, S. A. Quezada, D. Sproul, M. C. Frame, A. Serrels, S. M. Pollard, Glioblastomas acquire myeloid-affiliated transcriptional programs via epigenetic immunoediting to elicit immune evasion. *Cell* **184**, 2454-2470.e26 (2021).

18. R. Gao, B. He, Q. Huang, Z. Wang, M. Yan, E. W.-F. Lam, S. Lin, B. Wang, Q. Liu, Cancer cell immune mimicry delineates onco-immunologic modulation. *iScience* **24**, 103133 (2021).

19. C. E. Gast, A. D. Silk, L. Zarour, L. Riegler, J. G. Burkhart, K. T. Gustafson, M. S. Parappilly, M. Roh-Johnson, J. R. Goodman, B. Olson, M. Schmidt, J. R. Swain, P. S. Davies, V. Shasthri, S. Iizuka, P. Flynn, S. Watson, J. Korkola, S. A. Courtneidge, J. M. Fischer, J. Jaboin, K. G. Billingsley, C. D. Lopez, J. Burchard, J. Gray, L. M. Coussens, B. C. Sheppard, M. H. Wong, Cell fusion potentiates tumor heterogeneity and reveals circulating hybrid cells that correlate with stage and survival. *Sci Adv.* **4**, eaat7828 (2018).

20. F. A. Scheeren, A. H. Kuo, L. J. van Weele, S. Cai, I. Glykofridis, S. S. Sikandar, M. Zabala, D. Qian, J. S. Lam, D. Johnston, J. P. Volkmer, D. Sahoo, M. van de Rijn, F. M. Dirbas, G. Somlo, T. Kalisky, M. E. Rothenberg, S. R. Quake, M. F. Clarke, A cell-intrinsic role for TLR2–MYD88 in intestinal and breast epithelia and oncogenesis. *Nat Cell Biol.* **16**, 1238–1248 (2014).

21. Z. Liu, S. Chu, S. Yao, Y. Li, S. Fan, X. Sun, L. Su, X. Liu, CD74 interacts with CD44 and enhances tumorigenesis and metastasis via RHOA-mediated cofilin phosphorylation in human breast cancer cells. *Oncotarget* **7**, 68303–68313 (2016).

22. A. Müller, B. Homey, H. Soto, N. Ge, D. Catron, M. E. Buchanan, T. McClanahan, E. Murphy, W. Yuan, S. N. Wagner, J. L. Barrera, A. Mohar, E. Verástegui, A. Zlotnik, Involvement of chemokine receptors in breast cancer metastasis. *Nature* **410**, 50–56 (2001).

23. B. Pal, Y. Chen, F. Vaillant, B. D. Capaldo, R. Joyce, X. Song, V. L. Bryant, J. S. Penington, L. D. Stefano, N. T. Ribera, S. Wilcox, G. B. Mann, kConFab, A. T. Papenfuss, G. J. Lindeman, G. K. Smyth, J. E. Visvader, A single-cell RNA expression atlas of normal, preneoplastic and tumorigenic states in the human breast. *Embo J.* **40**, e107333 (2021).

24. S. Z. Wu, G. Al-Eryani, D. L. Roden, S. Junankar, K. Harvey, A. Andersson, A. Thennavan, C. Wang, J. R. Torpy, N. Bartonicek, T. Wang, L. Larsson, D. Kaczorowski, N. I. Weisenfeld, C. R. Uytingco, J. G. Chew, Z. W. Bent, C.-L. Chan, V. Gnanasambandapillai, C.-A. Dutertre, L. Gluch, M. N. Hui, J. Beith, A. Parker, E. Robbins, D. Segara, C. Cooper, C. Mak, B. Chan, S. Warrier, F. Ginhoux, E. Millar, J. E. Powell, S. R. Williams, X. S. Liu, S. O'Toole, E. Lim, J. Lundeberg, C. M. Perou, A. Swarbrick, A single-cell and spatially resolved atlas of human breast cancers. *Nat. Genet.* **53**, 1334–1347 (2021).

25. D. Cibrián, F. Sánchez-Madrid, CD69: from activation marker to metabolic gatekeeper. *Eur. J. Immunol.* **47**, 946–953 (2017).

26. L. K. Mackay, A. Braun, B. L. Macleod, N. Collins, C. Tebartz, S. Bedoui, F. R. Carbone, T. Gebhardt, Cutting edge: CD69 interference with sphingosine-1-phosphate receptor function regulates peripheral T cell retention. *J Immunol.* **194**, 2059–2063 (2015).

27. R. Satija, J. A. Farrell, D. Gennert, A. F. Schier, A. Regev, Spatial reconstruction of single-cell gene expression data. *Nat. Biotechnol.* **33**, 495–502 (2015).

28. C. S. McGinnis, L. M. Murrow, Z. J. Gartner, DoubletFinder: Doublet Detection in Single-Cell RNA Sequencing Data Using Artificial Nearest Neighbors. *Cell Syst.* **8**, 329-337.e4 (2019).

29. T. Tickle, I. Tirosh, C. Georgescu, M. Brown, B. Haas, inferCNV of the Trinity CTAT Project (2019).

30. T. Kumar, K. Nee, R. Wei, S. He, Q. H. Nguyen, S. Bai, K. Blake, M. Pein, Y. Gong, E. Sei, M. Hu, A. K. Casasent, A. Thennavan, J. Li, T. Tran, K. Chen, B. Nilges, N. Kashikar, O. Braubach, B. B. Cheikh, N. Nikulina, H. Chen, M. Teshome, B. Menegaz, H. Javaid, C. Nagi, J. Montalvan, T. Lev, S. Mallya, D. F. Tifrea, R. Edwards, E. Lin, R. Parajuli, S. Hanson, S. Winocour, A. Thompson, B. Lim, D. A. Lawson, K. Kessenbrock, N. Navin, A spatially resolved single-cell genomic atlas of the adult human breast. *Nature* **620**, 181–191 (2023).

31. E. Lim, D. Wu, B. Pal, T. Bouras, M.-L. Asselin-Labat, F. Vaillant, H. Yagita, G. J. Lindeman, G. K. Smyth, J. E. Visvader, Transcriptome analyses of mouse and human mammary

cell subpopulations reveal multiple conserved genes and pathways. *Breast Cancer Res.* **12**, R21 (2010).

32. K. Taniguchi, M. Karin, NF-κB, inflammation, immunity and cancer: coming of age. *Nat. Rev. Immunol.* **18**, 309–324 (2018).

33. M. Terekhova, A. Swain, P. Bohacova, E. Aladyeva, L. Arthur, A. Laha, D. A. Mogilenko, S. Burdess, V. Sukhov, D. Kleverov, B. Echalar, P. Tsurinov, R. Chernyatchik, K. Husarcikova, M. N. Artyomov, Single-cell atlas of healthy human blood unveils age-related loss of NKG2C+GZMB–CD8+ memory T cells and accumulation of type 2 memory T cells. *Immunity* **56**, 2836–2854 (2023).

34. A. Tsherniak, F. Vazquez, P. G. Montgomery, B. A. Weir, G. Kryukov, G. S. Cowley, S. Gill, W. F. Harrington, S. Pantel, J. M. Krill-Burger, R. M. Meyers, L. Ali, A. Goodale, Y. Lee, G. Jiang, J. Hsiao, W. F. J. Gerath, S. Howell, E. Merkel, M. Ghandi, L. A. Garraway, D. E. Root, T. R. Golub, J. S. Boehm, W. C. Hahn, Defining a Cancer Dependency Map. *Cell* **170**, 564-576.e16 (2017).

35. J. J. Engelhardt, B. Boldajipour, P. Beemiller, P. Pandurangi, C. Sorensen, Z. Werb, M. Egeblad, M. F. Krummel, Marginating Dendritic Cells of the Tumor Microenvironment Cross-Present Tumor Antigens and Stably Engage Tumor-Specific T Cells. *Cancer Cell* **21**, 402–417 (2012).

36. K. Murata, M. Inami, A. Hasegawa, S. Kubo, M. Kimura, M. Yamashita, H. Hosokawa, T. Nagao, K. Suzuki, K. Hashimoto, H. Shinkai, H. Koseki, M. Taniguchi, S. F. Ziegler, T. Nakayama, CD69-null mice protected from arthritis induced with anti-type II collagen antibodies. *Int. Immunol.* **15**, 987–992 (2003).

37. D. A. Walsh, H. B. da Silva, L. K. Beura, C. Peng, S. E. Hamilton, D. Masopust, S. C. Jameson, The Functional Requirement for CD69 in Establishment of Resident Memory CD8+ T Cells Varies with Tissue Location. *J. Immunol.* **203**, 946–955 (2019).

38. S. Koizume, T. Kanayama, Y. Kimura, H. Hirano, T. Takahashi, Y. Ota, K. Miyazaki, M. Yoshihara, Y. Nakamura, T. Yokose, H. Kato, K. Takenaka, S. Sato, H. Tadokoro, E. Miyagi, Y. Miyagi, Cancer cell-derived CD69 induced under lipid and oxygen starvation promotes ovarian cancer progression through fibronectin. *Cancer Sci.* **114**, 2485–2498 (2023).

39. T. Krausgruber, N. Fortelny, V. Fife-Gernedl, M. Senekowitsch, L. C. Schuster, A. Lercher, A. Nemc, C. Schmidl, A. F. Rendeiro, A. Bergthaler, C. Bock, Structural cells are key regulators of organ-specific immune responses. *Nature* **583**, 296–302 (2020).

40. D. G. DeNardo, D. J. Brennan, E. Rexhepaj, B. Ruffell, S. L. Shiao, S. F. Madden, W. M. Gallagher, N. Wadhwani, S. D. Keil, S. A. Junaid, H. S. Rugo, E. S. Hwang, K. Jirström, B. L. West, L. M. Coussens, Leukocyte Complexity Predicts Breast Cancer Survival and Functionally Regulates Response to Chemotherapy. *Cancer Discov.* **1**, 54–67 (2011).

41. B. Ruffell, A. Au, H. S. Rugo, L. J. Esserman, E. S. Hwang, L. M. Coussens, Leukocyte composition of human breast cancer. *Proc. Natl. Acad. Sci.* **109**, 2796–2801 (2012).

42. M. B. Lustberg, P. Balasubramanian, B. Miller, A. Garcia-Villa, C. Deighan, Y. Wu, S. Carothers, M. Berger, B. Ramaswamy, E. R. Macrae, R. Wesolowski, R. M. Layman, E. Mrozek, X. Pan, T. A. Summers, C. L. Shapiro, J. J. Chalmers, Heterogeneous atypical cell populations are present in blood of metastatic breast cancer patients. *Breast Cancer Res.* **16**, R23 (2014).

43. Z. Diamantopoulou, F. Castro-Giner, F. D. Schwab, C. Foerster, M. Saini, S. Budinjas, K. Strittmatter, I. Krol, B. Seifert, V. Heinzelmann-Schwarz, C. Kurzeder, C. Rochlitz, M. Vetter, W. P. Weber, N. Aceto, The metastatic spread of breast cancer accelerates during sleep. *Nature* **607**, 156–162 (2022).

44. A. N. Anderson, P. Conley, C. D. Klocke, S. K. Sengupta, A. Pang, H. C. Farley, A. R. Gillingham, A. D. Dawson, Y. Fan, J. A. Jones, S. L. Gibbs, A. H. Skalet, G. Wu, M. H. Wong, Detection of neoplastic-immune hybrid cells with metastatic properties in uveal melanoma. *Biomark. Res.* **12**, 67 (2024).

45. T. Chari, L. Pachter, The Specious Art of Single-Cell Genomics. *PLoS Comput. Biol.* ***17***, e1011288 (2022).

46. J. Oksanen, G. L. Simpson, F. G. Blanchet, R. Kindt, P. Legendre, P. R. Minchin, R. B. O'Hara, P. Solymos, M. H. H. Stevens, E. Szoecs, H. Wagner, M. Barbour, M. Bedward, B. Bolker, D. Borcard, T. Borman, G. Carvalho, M. Chirico, M. D. Caceres, S. Durand, H. B. A. Evangelista, R. FitzJohn, M. Friendly, B. Furneaux, G. Hannigan, M. O. Hill, L. Lahti, D. McGlinn, M.-H. Ouellette, E. R. Cunha, T. Smith, A. Stier, C. J. F. T. Braak, J. Weedon, vegan: Community Ecology Package. (2024; https://github.com/vegandevs/vegan, https://vegandevs.github.io/vegan/)

47. G. Korotkevich, V. Sukhov, N. Budin, B. Shpak, M. N. Artyomov, A. Sergushichev, Fast gene set enrichment analysis. *bioRxiv* https://doi.org/10.1101/060012 (2019).

48. A. Subramanian, P. Tamayo, V. K. Mootha, S. Mukherjee, B. L. Ebert, M. A. Gillette, A. Paulovich, S. L. Pomeroy, T. R. Golub, E. S. Lander, J. P. Mesirov, Gene set enrichment analysis: A knowledge-based approach for interpreting genome-wide expression profiles. *Proc. Natl. Acad. Sci.* **102**, 15545–15550 (2005).

49. T. Wei, V. Simko, "corrplot": Visualization of a Correlation Matrix. (2024; https://github.com/taiyun/corrplot).

50. L. Cassetta, S. Fragkogianni, A. H. Sims, A. Swierczak, L. M. Forrester, H. Zhang, D. Y. H. Soong, T. Cotechini, P. Anur, E. Y. Lin, A. Fidanza, M. Lopez-Yrigoyen, M. R. Millar, A. Urman, Z. Ai, P. T. Spellman, E. S. Hwang, J. M. Dixon, L. Wiechmann, L. M. Coussens, H. O. Smith, J. W. Pollard, Human Tumor-Associated Macrophage and Monocyte Transcriptional

Landscapes Reveal Cancer-Specific Reprogramming, Biomarkers, and Therapeutic Targets. *Cancer Cell* **35**, 588-602.e10 (2019).

51. T. Tsujikawa, S. Kumar, R. N. Borkar, V. Azimi, G. Thibault, Y. H. Chang, A. Balter, R. Kawashima, G. Choe, D. Sauer, E. E. Rassi, D. R. Clayburgh, M. F. Kulesz-Martin, E. R. Lutz, L. Zheng, E. M. Jaffee, P. Leyshock, A. A. Margolin, M. Mori, J. W. Gray, P. W. Flint, L. M. Coussens, Quantitative Multiplex Immunohistochemistry Reveals Myeloid-Inflamed Tumor-Immune Complexity Associated with Poor Prognosis. *Cell Rep.* **19**, 203–217 (2017).

52. T. M. Ashhurst, F. Marsh-Wakefield, G. H. Putri, A. G. Spiteri, D. Shinko, M. N. Read, A. L. Smith, N. J. C. King, Integration, exploration, and analysis of high-dimensional single-cell cytometry data using Spectre. *Cytom. A.* **101**, 237–253 (2022).

53. N. A. Kearns, R. M. J. Genga, M. S. Enuameh, M. Garber, S. A. Wolfe, R. Maehr, Cas9 effector-mediated regulation of transcription and differentiation in human pluripotent stem cells. *Development* **141**, 219–223 (2013).

54. S. Konermann, M. D. Brigham, A. E. Trevino, J. Joung, O. O. Abudayyeh, C. Barcena, P. D. Hsu, N. Habib, J. S. Gootenberg, H. Nishimasu, O. Nureki, F. Zhang, Genome-scale transcriptional activation by an engineered CRISPR-Cas9 complex. *Nature* **517**, 583–588 (2015).

55. J. Joung, S. Konermann, J. S. Gootenberg, O. O. Abudayyeh, R. J. Platt, M. D. Brigham, N. E. Sanjana, F. Zhang, Genome-scale CRISPR-Cas9 knockout and transcriptional activation screening. *Nat. Protoc.* **12**, 828–863 (2017).

56. M. Enomoto, M. B. Bunge, P. Tsoulfas, A multifunctional neurotrophin with reduced affinity to p75NTR enhances transplanted Schwann cell survival and axon growth after spinal cord injury. *Exp. Neurol.* **248**, 170–182 (2013).

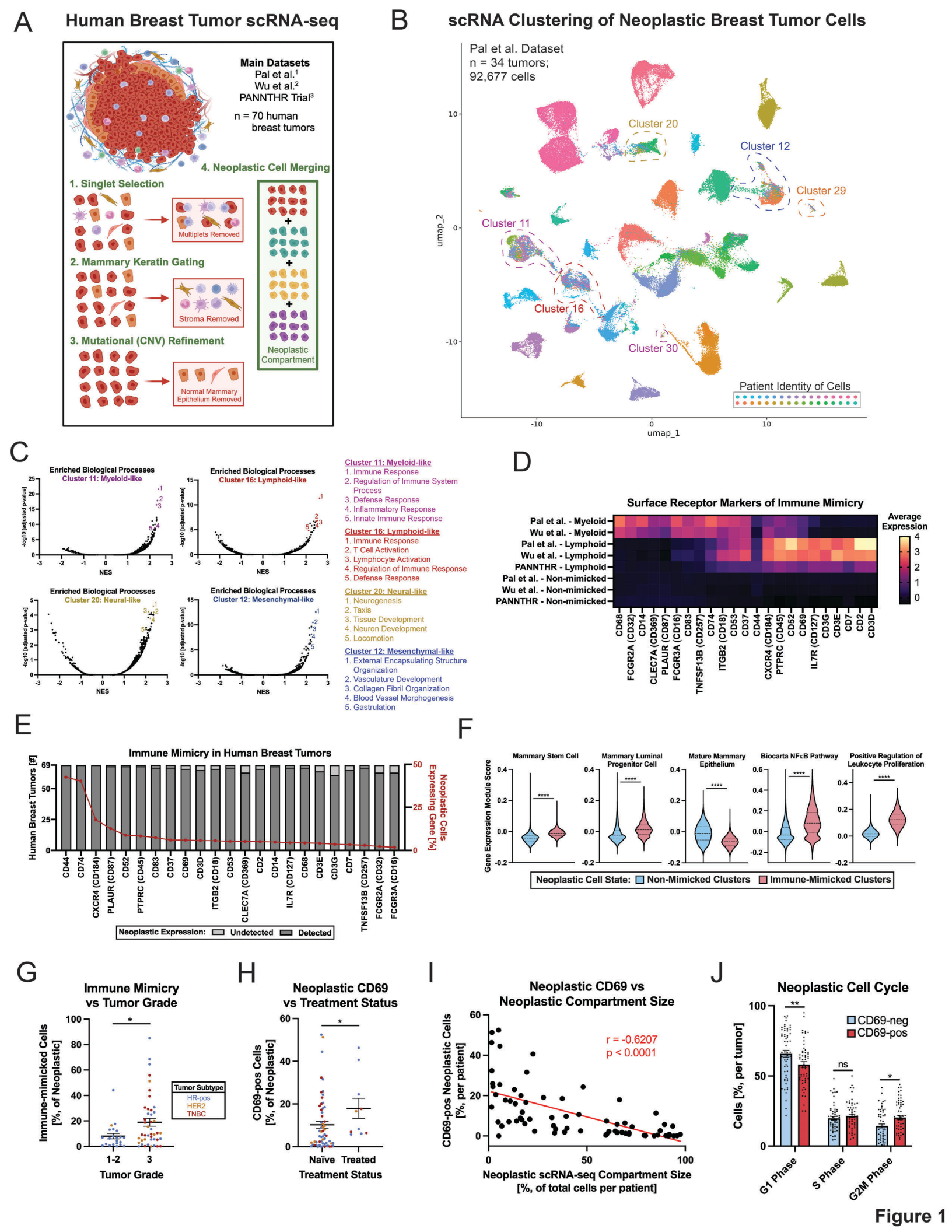
A
Human Breast Tumor scRNA-seq
Main Datasets
Pal et al.[1]
Wu et al.[2]
PANNTHR Trial[3]
n = 70 human breast tumors
4. Neoplastic Cell Merging
1. Singlet Selection
Multiplets Removed
2. Mammary Keratin Gating
Stroma Removed
3. Mutational (CNV) Refinement
Normal Mammary Epithelium Removed
Neoplastic Compartment
B
scRNA Clustering of Neoplastic Breast Tumor Cells
Pal et al. Dataset
n = 34 tumors;
92,677 cells
Cluster 20
Cluster 12
Cluster 29
Cluster 11
Cluster 16
Cluster 30
Patient Identity of Cells
umap_2
umap_1
C
Enriched Biological Processes
Cluster 11: Myeloid-like
Cluster 16: Lymphoid-like
Cluster 20: Neural-like
Cluster 12: Mesenchymal-like
-log10 [adjusted p-value]
NES
Cluster 11: Myeloid-like
1. Immune Response
2. Regulation of Immune System Process
3. Defense Response
4. Inflammatory Response
5. Innate Immune Response
Cluster 16: Lymphoid-like
1. Immune Response
2. T Cell Activation
3. Lymphocyte Activation
4. Regulation of Immune Response
5. Defense Response
Cluster 20: Neural-like
1. Neurogenesis
2. Taxis
3. Tissue Development
4. Neuron Development
5. Locomotion
Cluster 12: Mesenchymal-like
1. External Encapsulating Structure Organization
2. Vasculature Development
3. Collagen Fibril Organization
4. Blood Vessel Morphogenesis
5. Gastrulation
D
Surface Receptor Markers of Immune Mimicry
Pal et al. - Myeloid
Wu et al. - Myeloid
Pal et al. - Lymphoid
Wu et al. - Lymphoid
PANNTHR - Lymphoid
Pal et al. - Non-mimicked
Wu et al. - Non-mimicked
PANNTHR - Non-mimicked
Average Expression
CD68
FCGR2A (CD32)
CD14
CLEC7A (CD369)
PLAUR (CD87)
FCGR3A (CD16)
CD83
TNFSF13B (CD257)
CD74
ITGB2 (CD18)
CD53
CD37
CD44
CXCR4 (CD184)
PTPRC (CD45)
CD52
CD69
IL7R (CD127)
CD3G
CD3E
CD7
CD2
CD3D
E
Immune Mimicry in Human Breast Tumors
Human Breast Tumors [#]
Neoplastic Cells Expressing Gene [%]
Neoplastic Expression: Undetected Detected
F
Mammary Stem Cell
Mammary Luminal Progenitor Cell
Mature Mammary Epithelium
Biocarta NFκB Pathway
Positive Regulation of Leukocyte Proliferation
Gene Expression Module Score
Neoplastic Cell State: Non-Mimicked Clusters Immune-Mimicked Clusters
G
Immune Mimicry vs Tumor Grade
Immune-mimicked Cells [%, of Neoplastic]
Tumor Subtype
HR-pos
HER2
TNBC
Tumor Grade
H
Neoplastic CD69 vs Treatment Status
CD69-pos Cells [%, of Neoplastic]
Naïve
Treated
Treatment Status
I
Neoplastic CD69 vs Neoplastic Compartment Size
r = -0.6207
p < 0.0001
CD69-pos Neoplastic Cells [%, per patient]
Neoplastic scRNA-seq Compartment Size [%, of total cells per patient]
J
Neoplastic Cell Cycle
CD69-neg
CD69-pos
Cells [%, per tumor]
G1 Phase
S Phase
G2M Phase

Figure 1

Figure 1. Neoplastic immune mimicry is identified in independent human breast tumor scRNA-seq cohorts. (**A**) scRNA-seq workflow to collect neoplastic cells based on mammary keratin gene expression. (**B**) Example of scRNA-seq clustering from the Pal *et al*. dataset where cells are colored according to their patient identity. Indicated clusters depict neoplastic cell states shared across patients that (**C**) express myeloid-like, lymphoid-like, neural-like, and mesenchymal-like gene signatures. (**D**) Immune mimicry is signified by neoplastic cells expressing canonical leukocyte surface receptor genes in a concordant manner across distinct scRNA-seq datasets. (**E**) The vast majority of breast tumors analyzed have neoplastic cells expressing these immune mimicry markers as a minority subpopulation. (**F**) Neoplastic cells found within immune-like scRNA-seq clusters are enriched for dedifferentiated, NFκB pathway, and proliferative gene signatures. (**G**) Neoplastic immune mimicry is elevated in high-grade breast tumors. (**H**) Neoplastic cells expressing the CD69 early activation marker are increased in tumors subjected to therapy before surgical resection, (**I**) in scRNA-seq samples harboring a smaller epithelial compartment, and (**J**) they are more often classified as mitotic. * $p < 0.05$; ** $p < 0.01$; **** $p < 0.0001$. Wilcoxon signed-rank test (F), Mann-Whitney test [(G) and (H)], Pearson correlation (I) or two-way ANOVA with Šidák correction (J). Data are means ± SEM.

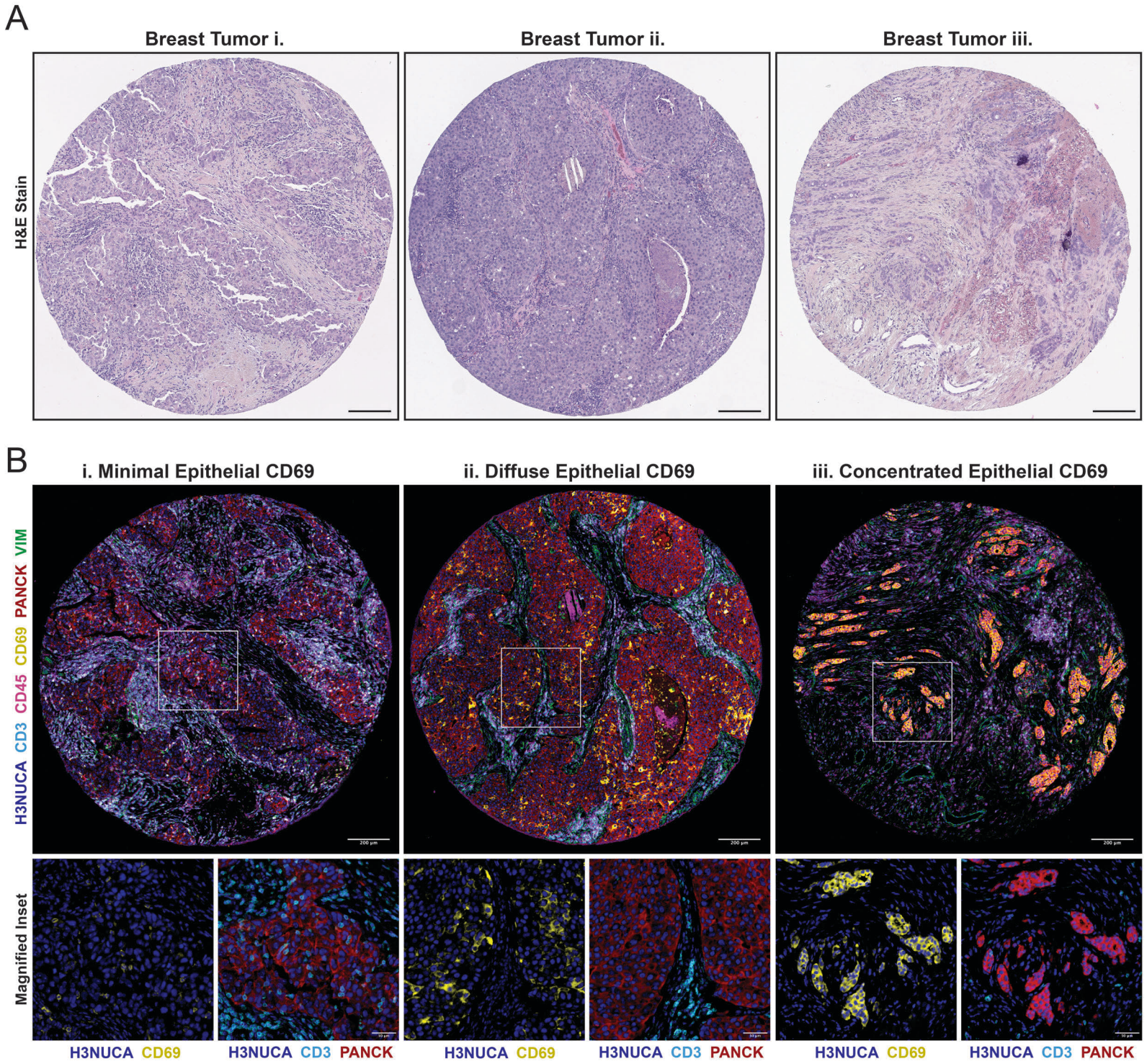
A
Breast Tumor i.
Breast Tumor ii.
Breast Tumor iii.
H&E Stain
B
i. Minimal Epithelial CD69
ii. Diffuse Epithelial CD69
iii. Concentrated Epithelial CD69
H3NUCA CD3 CD45 CD69 PANCK VIM
Magnified Inset
H3NUCA CD69
H3NUCA CD3 PANCK
H3NUCA CD69
H3NUCA CD3 PANCK
H3NUCA CD69
H3NUCA CD3 PANCK
C
Histopathological Epithelial CD69 Across Breast Tumors
CD69 Positivity
[%, of panCK-pos per tumor]
20
15
10
5
0
Subtype
Luminal
HER2
TNBC
Treatment
Naïve
Treated
Average = 1.9%
Examples Above
i.
Tumor Grade:
1
2
3
ii.
iii.

Figure 2

Figure 2. The immune mimicry CD69 marker is associated with aggressive breast cancer in histopathological samples. (**A**) Hematoxylin and Eosin (H&E) staining of human breast tumors. These same tissues were subsequently subjected to multiplexed immunohistochemistry to detect epithelial CD69. Scale bar, 200 μm. (**B**) Multiplexed immunohistochemistry examples of epithelial CD69 or the lack thereof in primary human breast tumors. Epithelial CD69 is denoted by overlapping PANCK (red) and CD69 (yellow). The first example portrays a lack of epithelial CD69 amid immune cell (CD3-pos, cyan) expression. The second and third examples show epithelial CD69 in diffuse and concentrated staining patterns, respectively. Scale bar, 200 μm. The insets provide magnified views of CD69 (left) versus CD3 and pan-cytokeratin (right). Inset Scale bar, 50 μm. (**C**) Numerous human breast tumors have detectable levels of epithelial CD69. Plot depicts the percent of epithelial cells strongly positive for CD69 for distinct tumors along with clinical parameters. Epithelial CD69 is summarized from a conservative gating approach applied to multiple regions in 58 tumors.

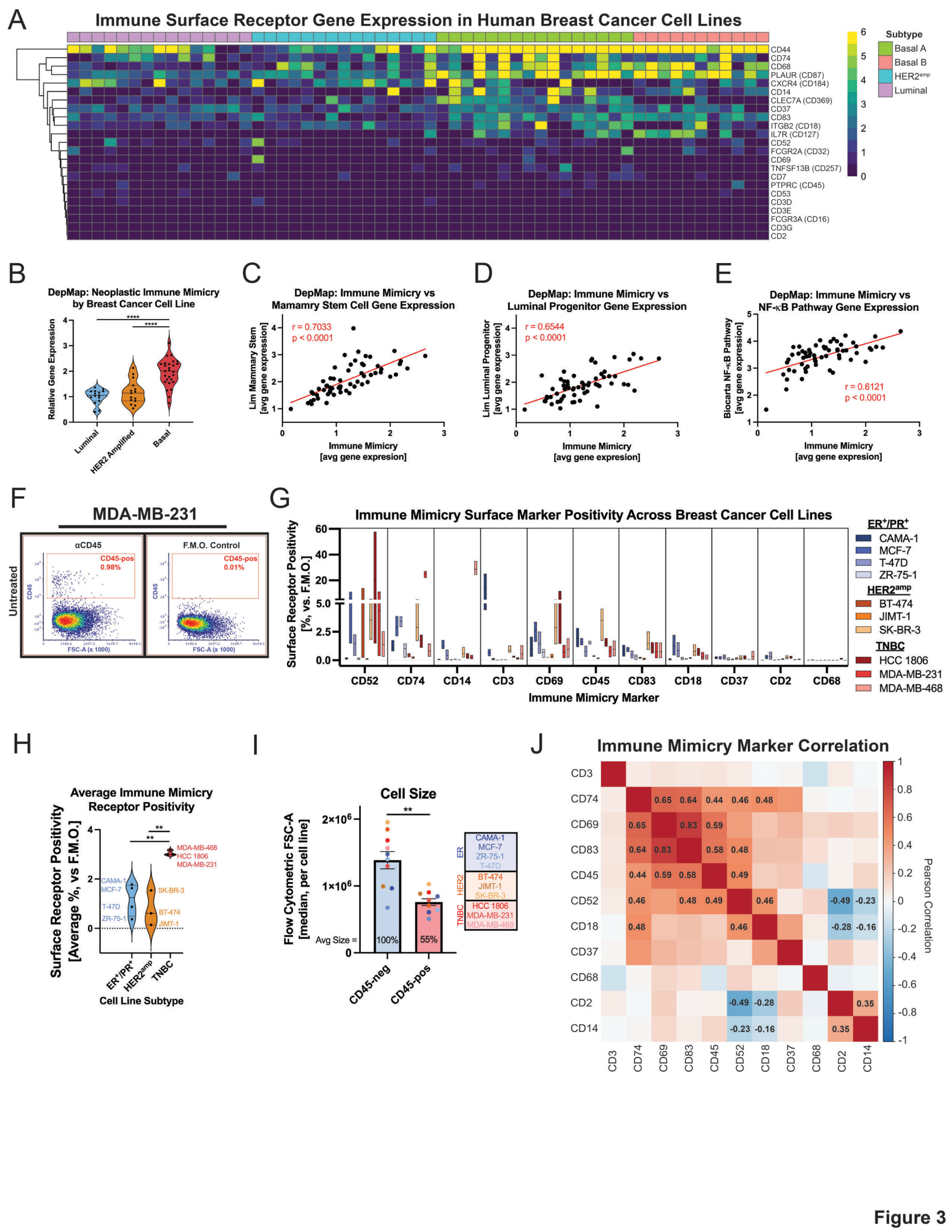
A
Immune Surface Receptor Gene Expression in Human Breast Cancer Cell Lines
Subtype
Basal A
Basal B
HER2amp
Luminal
CD44
CD74
CD68
PLAUR (CD87)
CXCR4 (CD184)
CD14
CLEC7A (CD369)
CD37
CD83
ITGB2 (CD18)
IL7R (CD127)
CD52
FCGR2A (CD32)
CD69
TNFSF13B (CD257)
CD7
PTPRC (CD45)
CD53
CD3D
CD3E
FCGR3A (CD16)
CD3G
CD2
B
DepMap: Neoplastic Immune Mimicry by Breast Cancer Cell Line
Relative Gene Expression
Luminal
HER2 Amplified
Basal
C
DepMap: Immune Mimicry vs Mamamry Stem Cell Gene Expression
r = 0.7033
p < 0.0001
Lim Mammary Stem [avg gene expression]
Immune Mimicry [avg gene expresion]
D
DepMap: Immune Mimicry vs Luminal Progenitor Gene Expression
r = 0.6544
p < 0.0001
Lim Luminal Progenitor [avg gene expression]
Immune Mimicry [avg gene expresion]
E
DepMap: Immune Mimicry vs NF-κB Pathway Gene Expression
r = 0.6121
p < 0.0001
Biocarta NF-κB Pathway [avg gene expression]
Immune Mimicry [avg gene expresion]
F
MDA-MB-231
Untreated
αCD45
CD45-pos 0.98%
F.M.O. Control
CD45-pos 0.01%
FSC-A (x 1000)
G
Immune Mimicry Surface Marker Positivity Across Breast Cancer Cell Lines
Surface Receptor Positivity [%, vs. F.M.O.]
ER+/PR+
CAMA-1
MCF-7
T-47D
ZR-75-1
HER2amp
BT-474
JIMT-1
SK-BR-3
TNBC
HCC 1806
MDA-MB-231
MDA-MB-468
CD52
CD74
CD14
CD3
CD69
CD45
CD83
CD18
CD37
CD2
CD68
Immune Mimicry Marker
H
Average Immune Mimicry Receptor Positivity
Surface Receptor Positivity [Average %, vs F.M.O.]
MDA-MB-468
HCC 1806
MDA-MB-231
CAMA-1
MCF-7
T-47D
ZR-75-1
SK-BR-3
BT-474
JIMT-1
ER+/PR+
HER2amp
TNBC
Cell Line Subtype
I
Cell Size
Flow Cytometric FSC-A [median, per cell line]
Avg Size =
100%
55%
CD45-neg
CD45-pos
ER
HER2
TNBC
J
Immune Mimicry Marker Correlation
Pearson Correlation

Figure 3

Figure 3. Breast cancer cell lines express leukocyte surface receptor RNA and protein. (**A**) Interrogation of immune mimicry gene expression in public bulk RNA-seq DepMap data encompassing 57 breast cancer cell lines. (**B**) Neoplastic immune mimicry RNA gene expression is highest in breast cancer cell lines of the basal phenotype. Breast cancer cell lines expressing greater levels of leukocyte surface receptor genes positively correlate with (**C**) mammary stem, (**D**) mammary luminal progenitor, and (**E**) NFκB pathway gene signatures. (**F**) Example of flow cytometric CD45 protein staining in MDA-MB-231 cells. Negative (fluorescence minus one) control shown for comparison. (**G**) Demonstration of canonical leukocyte surface receptor protein positivity in 10 human breast cancer cell lines via flow cytometry. Data are monostains performed in biological triplicate. (**H**) Triple-negative breast cancer cell lines exhibit greater levels of leukocyte surface receptor protein. (**I**) Immune-mimicked CD45-pos cells are significantly smaller than CD45-neg cells. (**J**) Immune mimicry marker correlations across the 10 cell lines subjected to the flow cytometry analysis. Coefficients for significant correlations are indicated. ** $p < 0.01$; **** $p < 0.0001$. One-way ANOVA with Tukey correction [(B) and (H)], Pearson correlation [(C), (D), (E) and (J)], or Wilcoxon signed-rank test (I). Data are means ± SEM.

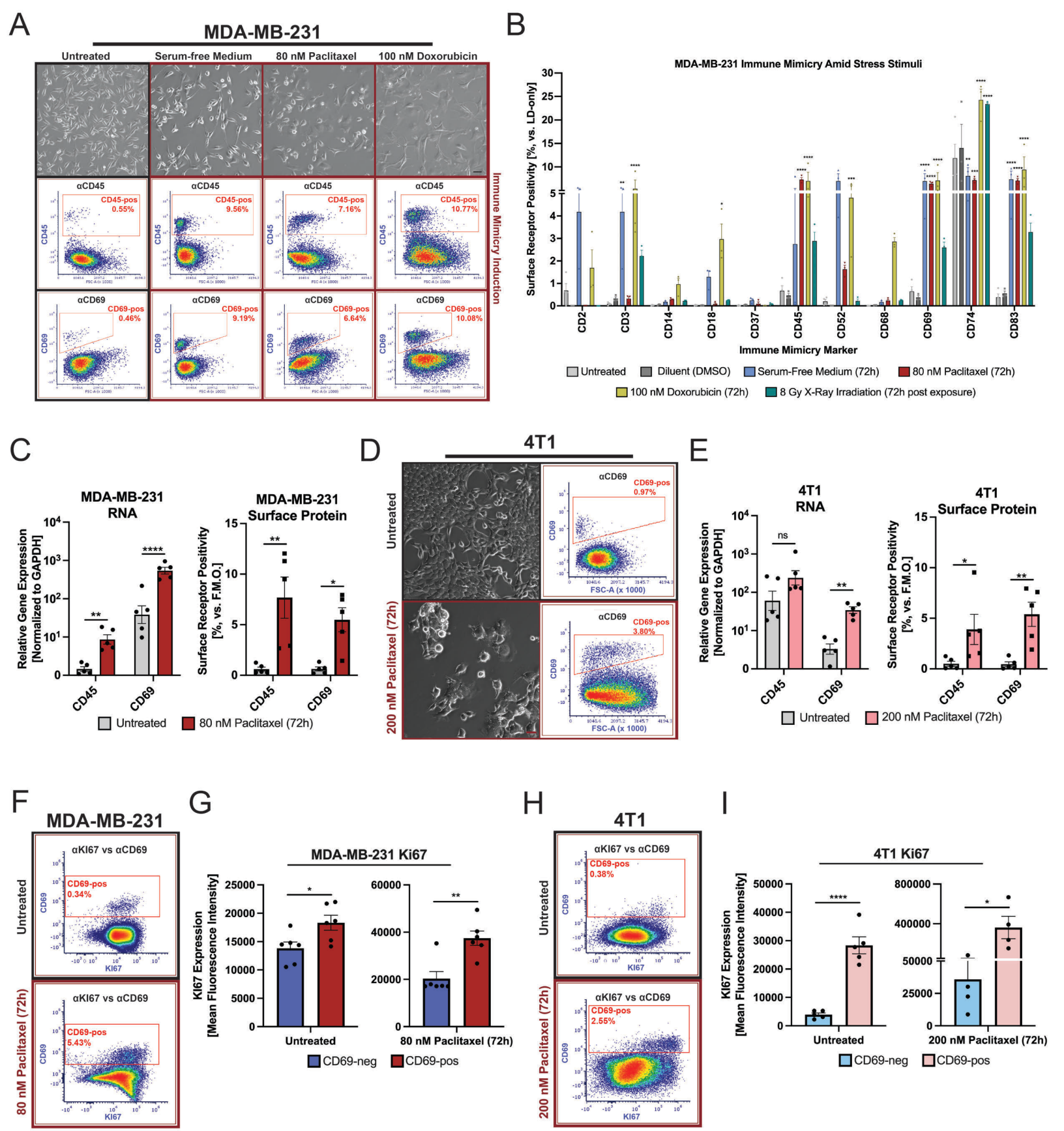
A
MDA-MB-231
Untreated
Serum-free Medium
80 nM Paclitaxel
100 nM Doxorubicin
αCD45
CD45-pos 0.55%
CD45-pos 9.56%
CD45-pos 7.16%
CD45-pos 10.77%
αCD69
CD69-pos 0.46%
CD69-pos 9.19%
CD69-pos 6.64%
CD69-pos 10.08%
Immune Mimicry Induction
B
MDA-MB-231 Immune Mimicry Amid Stress Stimuli
Surface Receptor Positivity [%, vs. LD-only]
CD2
CD3
CD14
CD18
CD37
CD45
CD52
CD68
CD69
CD74
CD83
Immune Mimicry Marker
Untreated
Diluent (DMSO)
Serum-Free Medium (72h)
80 nM Paclitaxel (72h)
100 nM Doxorubicin (72h)
8 Gy X-Ray Irradiation (72h post exposure)
C
MDA-MB-231 RNA
Relative Gene Expression [Normalized to GAPDH]
MDA-MB-231 Surface Protein
Surface Receptor Positivity [%, vs. F.M.O.]
CD45
CD69
Untreated
80 nM Paclitaxel (72h)
D
4T1
Untreated
200 nM Paclitaxel (72h)
αCD69
CD69-pos 0.97%
CD69-pos 3.80%
FSC-A (x 1000)
E
4T1 RNA
4T1 Surface Protein
ns
Untreated
200 nM Paclitaxel (72h)
F
MDA-MB-231
αKI67 vs αCD69
CD69-pos 0.34%
CD69-pos 5.43%
KI67
G
MDA-MB-231 Ki67
KI67 Expression [Mean Fluorescence Intensity]
Untreated
80 nM Paclitaxel (72h)
CD69-neg
CD69-pos
H
4T1
CD69-pos 0.38%
CD69-pos 2.55%
I
4T1 Ki67
200 nM Paclitaxel (72h)

Figure 4

Figure 4. Cytotoxic therapy further induces neoplastic immune mimicry and CD69. (**A**) Cell stress stimuli robustly expand the subpopulation of cells expressing CD45 and CD69 in MDA-MB-231. Scale bar, 50 μm. (**B**) Example of immune surface receptor positivity for MDA-MB-231 cells across various cytotoxic conditions. Data represent flow cytometric all stains done in biological triplicate. (**C**) CD45 and CD69 are induced at the RNA and protein level in MDA-MB-231 in response to paclitaxel. Data are biological replicates with surface protein measured as FACS monostains. (**D**) FACS example of paclitaxel treatment expanding the CD69-pos subpopulation in murine mammary 4T1 cells. Scale bar, 25 μm. (**E**) CD45 and CD69 are transcriptionally elevated in 4T1 cells following paclitaxel treatment. Data are biological replicates with surface protein measured as FACS monostains. (**F**-**G**) CD69-pos MDA-MB-231 cells express higher levels of KI67 in untreated and paclitaxel-treated culture conditions. Data are biological replicates. (**H**-**I**) CD69-pos MDA-MB-231 cells express higher levels of KI67 in untreated and paclitaxel-treated culture conditions. Data are biological replicates. * $p < 0.05$; ** $p < 0.01$; *** $p < 0.001$; **** $p < 0.0001$. Two-way ANOVA with Dunnett correction (B) or Šidák correction [(C) and (E)], or Student's t-test [(G) and (I)] Data are means ± SEM.

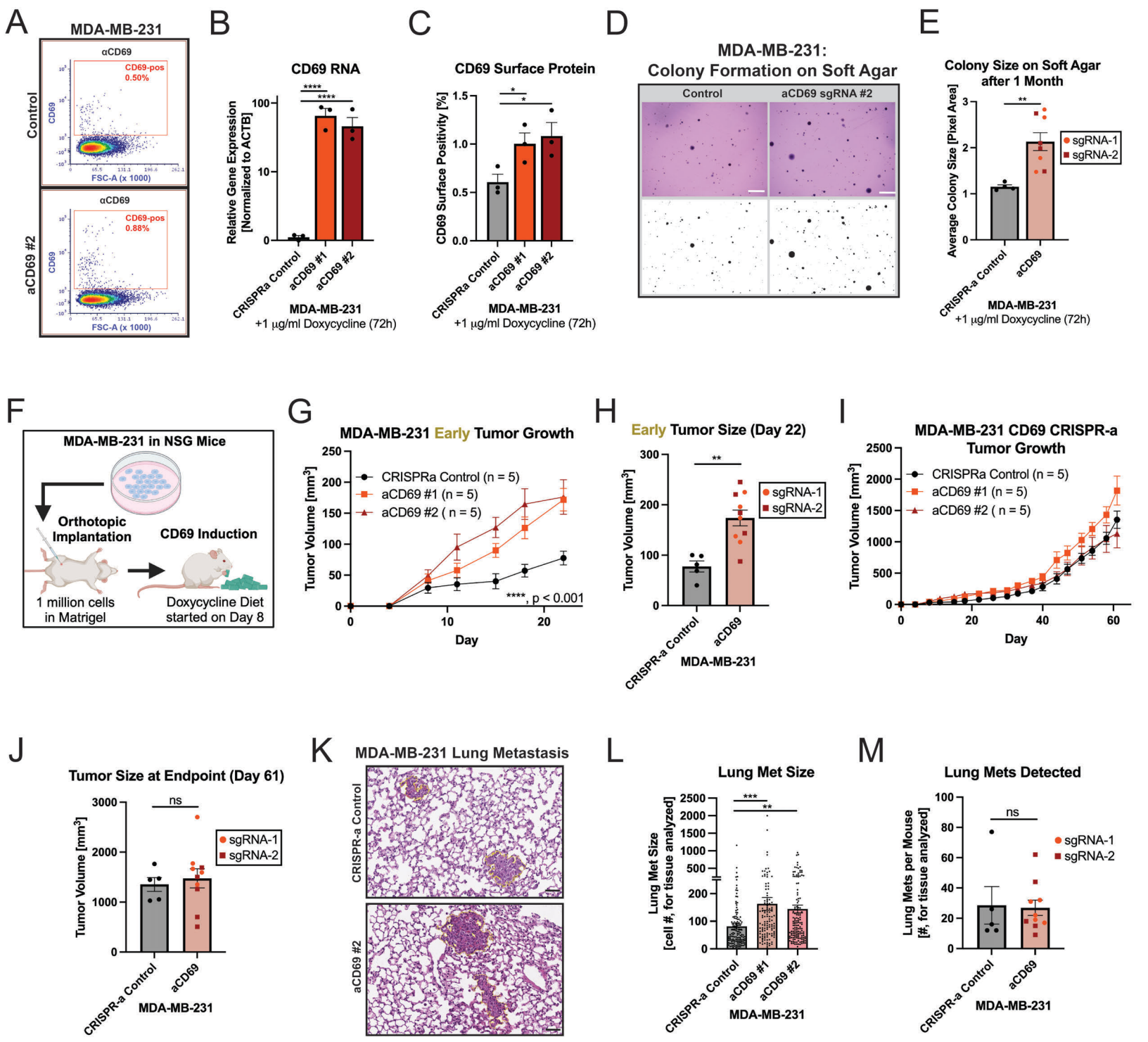
A
MDA-MB-231
αCD69
CD69-pos
0.50%
Control
CD69
FSC-A (x 1000)
αCD69
CD69-pos
0.88%
aCD69 #2
CD69
FSC-A (x 1000)
B
CD69 RNA
Relative Gene Expression [Normalized to ACTB]
****
****
CRISPRa Control
aCD69 #1
aCD69 #2
MDA-MB-231
+1 μg/ml Doxycycline (72h)
C
CD69 Surface Protein
CD69 Surface Positivity [%]
*
*
CRISPRa Control
aCD69 #1
aCD69 #2
MDA-MB-231
+1 μg/ml Doxycycline (72h)
D
MDA-MB-231:
Colony Formation on Soft Agar
Control
aCD69 sgRNA #2
E
Colony Size on Soft Agar after 1 Month
Average Colony Size [Pixel Area]
**
sgRNA-1
sgRNA-2
CRISPR-a Control
aCD69
MDA-MB-231
+1 μg/ml Doxycycline (72h)
F
MDA-MB-231 in NSG Mice
Orthotopic Implantation
CD69 Induction
1 million cells in Matrigel
Doxycycline Diet started on Day 8
G
MDA-MB-231 Early Tumor Growth
Tumor Volume [mm³]
CRISPRa Control (n = 5)
aCD69 #1 (n = 5)
aCD69 #2 (n = 5)
****, p < 0.001
Day
H
Early Tumor Size (Day 22)
Tumor Volume [mm³]
**
sgRNA-1
sgRNA-2
CRISPR-a Control
aCD69
MDA-MB-231
I
MDA-MB-231 CD69 CRISPR-a Tumor Growth
Tumor Volume [mm³]
CRISPRa Control (n = 5)
aCD69 #1 (n = 5)
aCD69 #2 (n = 5)
Day
J
Tumor Size at Endpoint (Day 61)
Tumor Volume [mm³]
ns
sgRNA-1
sgRNA-2
CRISPR-a Control
aCD69
MDA-MB-231
K
MDA-MB-231 Lung Metastasis
CRISPR-a Control
aCD69 #2
L
Lung Met Size
Lung Met Size [cell #, for tissue analyzed]
***
**
CRISPR-a Control
aCD69 #1
aCD69 #2
MDA-MB-231
M
Lung Mets Detected
Lung Mets per Mouse [#, for tissue analyzed]
ns
sgRNA-1
sgRNA-2
CRISPR-a Control
aCD69
MDA-MB-231

Figure 5

Figure 5. MDA-MB-231 cells overexpressing CD69 exhibit increased growth at low density *in vitro* and in mice. (**A**) CRISPR-activation of CD69 via doxycycline exposure in MDA-MB-231 increases its (**B**) RNA and (**C**) surface protein expression. (**D-E**) CD69-activated MDA-MB-231 cells form larger colonies when plated at low density on soft-agar. Scale bar, 2 mm. (**F**) MDA-MB-231 cells were orthotopically implanted into NSG mice for a tumor growth and metastasis assay. Mice were subsequently fed a doxycycline diet on day 8 to induce CD69 in implanted cells. (**G-H**) CD69-activated MDA-MB-231 cells demonstrated enhanced early tumor growth that (**I-J**) abated by the study endpoint. (**K**) At endpoint, NSG mice implanted with CD69-activated MDA-MB-231 cells had lung metastases that (**L**) were larger but (M) not more numerous. Scale bar, 50 μm. ns = not significant, * $p < 0.05$; ** $p < 0.01$; *** $p < 0.001$; **** $p < 0.0001$. One-way ANOVA with Tukey correction [(B) and (C)] or Dunnett correction (L), Student's t-test [(E), (H) and (J)], two-way ANOVA [(G) and (I)], or Mann-Whitney test (M). Data are means ± SEM.

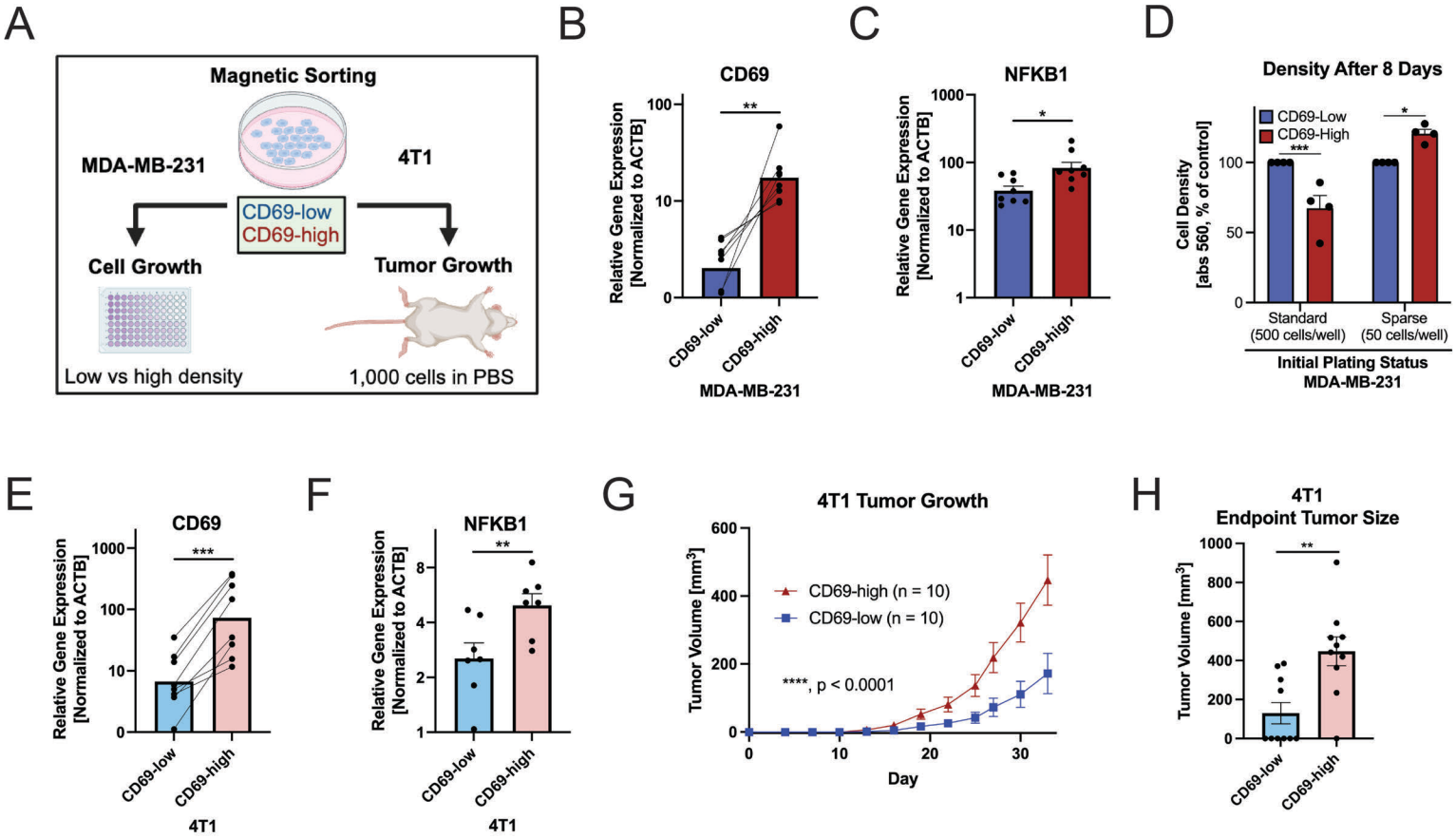
A
Magnetic Sorting
MDA-MB-231
4T1
CD69-low
CD69-high
Cell Growth
Tumor Growth
Low vs high density
1,000 cells in PBS
B
CD69
Relative Gene Expression [Normalized to ACTB]
CD69-low
CD69-high
MDA-MB-231
C
NFKB1
Relative Gene Expression [Normalized to ACTB]
CD69-low
CD69-high
MDA-MB-231
D
Density After 8 Days
CD69-Low
CD69-High
Cell Density [abs 560, % of control]
Standard (500 cells/well)
Sparse (50 cells/well)
Initial Plating Status
MDA-MB-231
E
CD69
Relative Gene Expression [Normalized to ACTB]
CD69-low
CD69-high
4T1
F
NFKB1
Relative Gene Expression [Normalized to ACTB]
CD69-low
CD69-high
4T1
G
4T1 Tumor Growth
Tumor Volume [mm3]
CD69-high (n = 10)
CD69-low (n = 10)
****, p < 0.0001
Day
H
4T1
Endpoint Tumor Size
Tumor Volume [mm3]
CD69-low
CD69-high

Figure 6

Figure 6. MDA-MB-231 and 4T1 cells magnetically sorted for CD69 grow more efficiently at low density *in vitro* and in mice. (**A**) MDA-MB-231 and 4T1 cells were magnetically sorted into CD69-low and CD69-high fractions. Sorting 200 million cells from each cell line yielded, on average, around 50,000 CD69-high cells that were subjected to enrichment validation via qRT-PCR. MDA-MB-231 sorted populations were used for *in vitro* growth assays whereas 4T1 populations were assessed for tumor growth at low density in syngeneic BALB/c mice. MDA-MB-231 cells were enriched for (**B**) CD69 and (**C**) NFKB1 RNA expression. (**D**) Subjecting these CD69-sorted MDA-MB-231 subpopulations to an *in vitro* growth assay revealed enhanced density by the CD69-high fraction when plated sparsely. (**E**) The 4T1 CD69-high fraction was enriched for CD69 and (**F**) NFKB1 RNA expression. (**G**) CD69-high 4T1 cells more efficiently form tumors when injected into BALB/c mice at low density with (**H**) tumors reaching a larger size at endpoint. * $p < 0.05$; ** $p < 0.01$; *** $p < 0.001$; **** $p < 0.0001$. Student's t-test [(B), (C), (E), (F) and (H)], or two-way ANOVA (G) with Šidák correction (D). Data are means ± SEM.

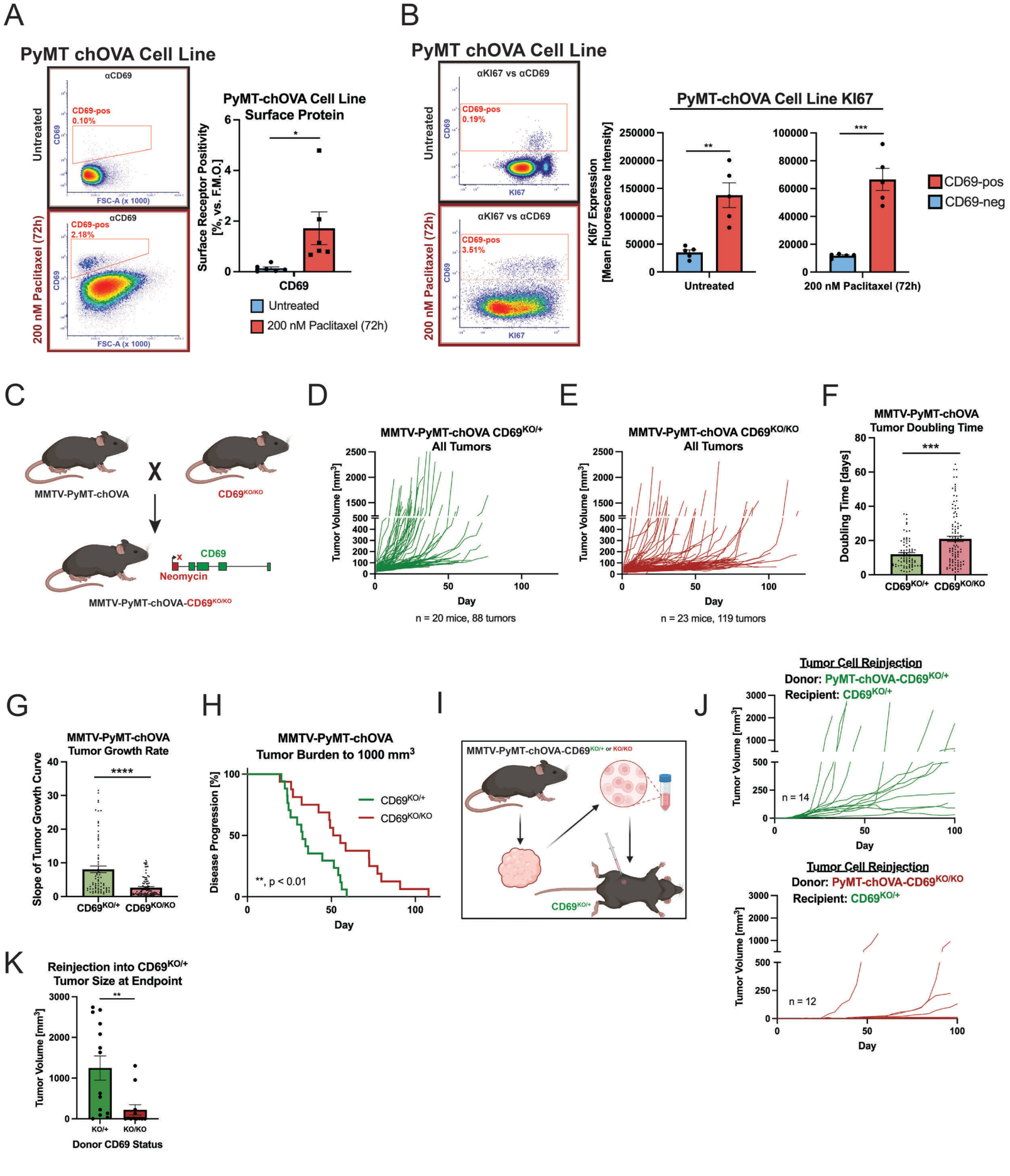
A
PyMT chOVA Cell Line
αCD69
Untreated
CD69-pos
0.10%
CD69
FSC-A (x 1000)
200 nM Paclitaxel (72h)
CD69-pos
2.18%
PyMT-chOVA Cell Line
Surface Protein
Surface Receptor Positivity
[%, vs. F.M.O.]
CD69
Untreated
200 nM Paclitaxel (72h)
B
PyMT chOVA Cell Line
αKI67 vs αCD69
CD69-pos
0.19%
KI67
CD69-pos
3.51%
PyMT-chOVA Cell Line KI67
KI67 Expression
[Mean Fluorescence Intensity]
Untreated
200 nM Paclitaxel (72h)
CD69-pos
CD69-neg
C
MMTV-PyMT-chOVA
CD69KO/KO
Neomycin
CD69
MMTV-PyMT-chOVA-CD69KO/KO
D
MMTV-PyMT-chOVA CD69KO/+
All Tumors
Tumor Volume [mm3]
Day
n = 20 mice, 88 tumors
E
MMTV-PyMT-chOVA CD69KO/KO
All Tumors
Tumor Volume [mm3]
Day
n = 23 mice, 119 tumors
F
MMTV-PyMT-chOVA
Tumor Doubling Time
Doubling Time [days]
CD69KO/+
CD69KO/KO
G
MMTV-PyMT-chOVA
Tumor Growth Rate
Slope of Tumor Growth Curve
CD69KO/+
CD69KO/KO
H
MMTV-PyMT-chOVA
Tumor Burden to 1000 mm3
Disease Progression [%]
CD69KO/+
CD69KO/KO
**, p < 0.01
Day
I
MMTV-PyMT-chOVA-CD69KO/+ or KO/KO
CD69KO/+
J
Tumor Cell Reinjection
Donor: PyMT-chOVA-CD69KO/+
Recipient: CD69KO/+
Tumor Volume [mm3]
n = 14
Day
Tumor Cell Reinjection
Donor: PyMT-chOVA-CD69KO/KO
Recipient: CD69KO/+
Tumor Volume [mm3]
n = 12
Day
K
Reinjection into CD69KO/+
Tumor Size at Endpoint
Tumor Volume [mm3]
KO/+
KO/KO
Donor CD69 Status

Figure 7

Figure 7. Knockout of CD69 in MMTV-PyMT-chOVA mice attenuates early tumor growth. (**A**) A cell line derived from an MMTV-PyMT-chOVA tumor has a CD69-pos subpopulation that expands upon paclitaxel treatment and (**B**) upregulates KI67. (**C**) MMTV-PyMT-chOVA mice were bred with CD69-knockout mice to generate MMTV-PyMT-chOVA-CD69$^{KO/KO}$ mice. (**D-E**) Comparing spontaneous tumor growth in PyMT-chOVA-CD69$^{KO/+}$ versus MMTV-PyMT-chOVA-CD69$^{KO/KO}$ mice uncovers (**F**) increased tumor doubling time and (**G**) slower rate in the latter. (**H**) MMTV-PyMT-chOVA-CD69$^{KO/KO}$ mice take longer to achieve a tumor burden of 1000 mm^3 when compared to mice harboring intact CD69. (**I**) Tumor cells were dissociated from MMTV-PyMT-chOVA-CD69$^{KO/+}$ and MMTV-PyMT-chOVA-CD69$^{KO/KO}$ mice for orthotopic reinjection back into standard CD69$^{KO/+}$ mice. (**J**) MMTV-PyMT-chOVA-CD69$^{KO/+}$ tumor cells are better able to grow upon reinjection into CD69$^{KO/+}$ mice and (**K**) attain larger tumors by study endpoint. * $p < 0.05$; ** $p < 0.01$; *** $p < 0.001$; **** $p < 0.0001$. Student's t-test [(A), (B) and (K)], Mann-Whitney test [(F) and (G)], or Mantel-Cox log-rank test (H).

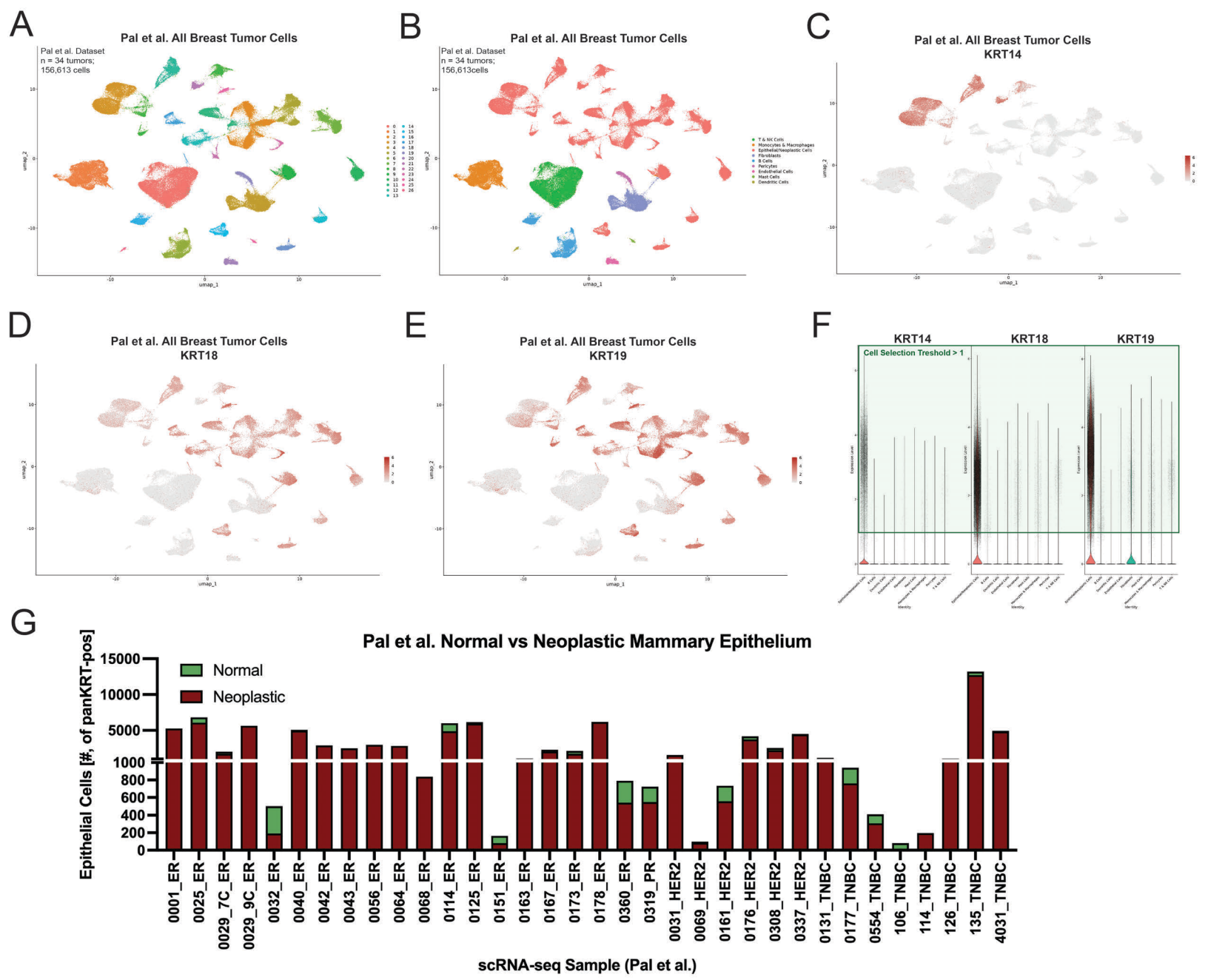

Supplementary Figure 1

Supplementary Figure 1. Collection of cells expressing mammary keratins and identification of neoplastic compartment in the Pal *et al.* human breast tumor scRNA-seq dataset. (**A**) Umap plot depicting all cells identified in the Pal *et al.* scRNA-seq dataset and (**B**) their conventional cell type assignments. Cells expressing mammary keratins (**C**) KRT14 (**D**) KRT18 and (**E**) KRT19 are located outside the main epithelial clusters. (**F**) Cells expressing mammary keratins were collected for downstream analysis regardless of cluster location using a threshold gating approach. (**G**) Neoplastic cells with inferred CNVs were refined from the epithelial pool. Normal epithelial cells showed parity with an epithelial reference generated from reduction mammoplasties and were hence omitted from downstream analysis.

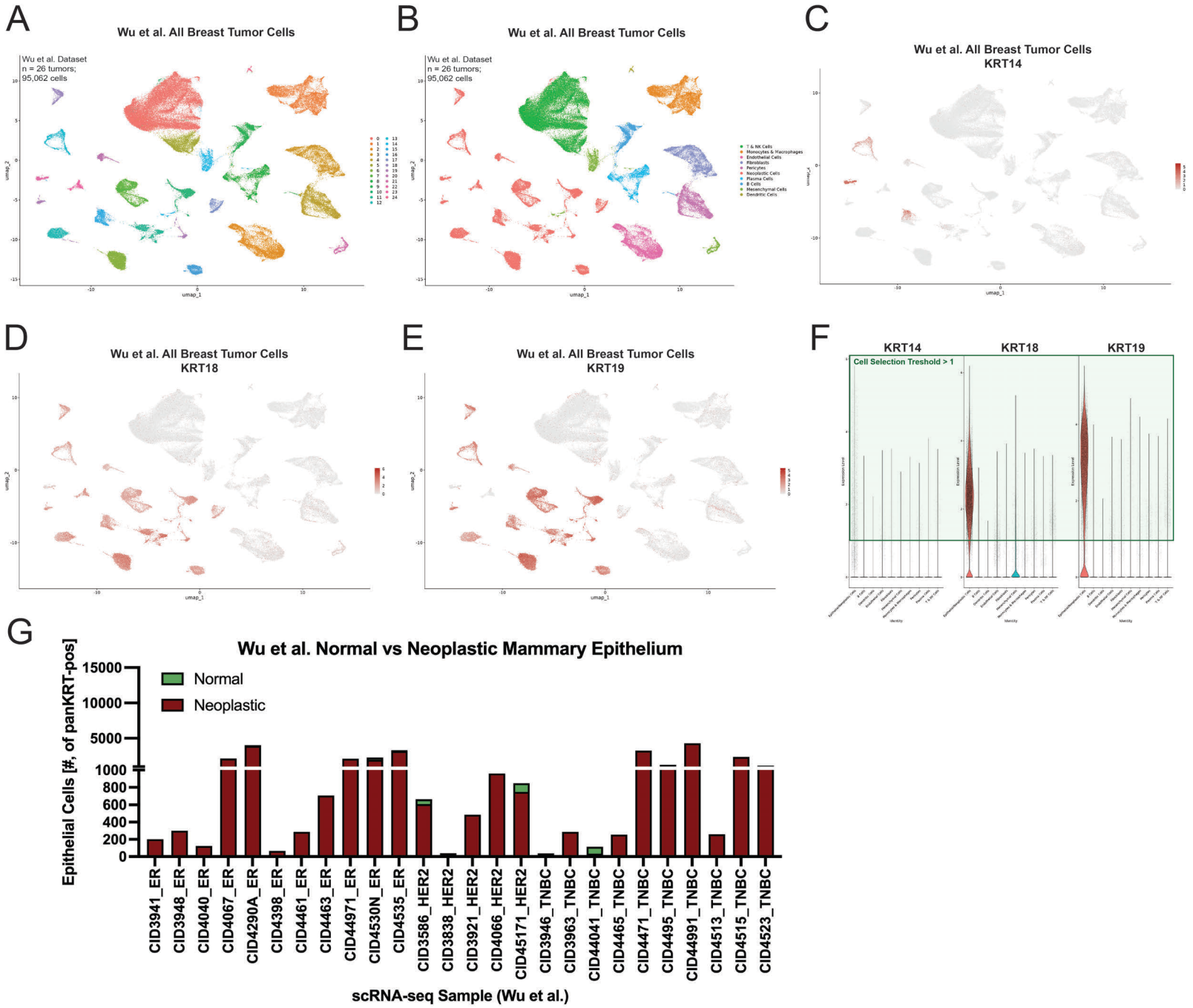

Supplementary Figure 2

Supplementary Figure 2. Collection of cells expressing mammary keratins and identification of neoplastic compartment in the Wu *et al.* human breast tumor scRNA-seq dataset. (**A**) Umap plot depicting all cells identified in the Wu *et al.* scRNA-seq dataset and (**B**) their conventional cell type assignments. Cells expressing mammary keratins (**C**) KRT14 (**D**) KRT18 and (**E**) KRT19 are located outside the main epithelial clusters. (**F**) Cells expressing mammary keratins were collected for downstream analysis regardless of cluster location using a threshold gating approach. (**G**) Neoplastic cells with inferred CNVs were refined from the epithelial pool. Normal epithelial cells showed parity with an epithelial reference generated from reduction mammoplasties and were hence omitted from downstream analysis.

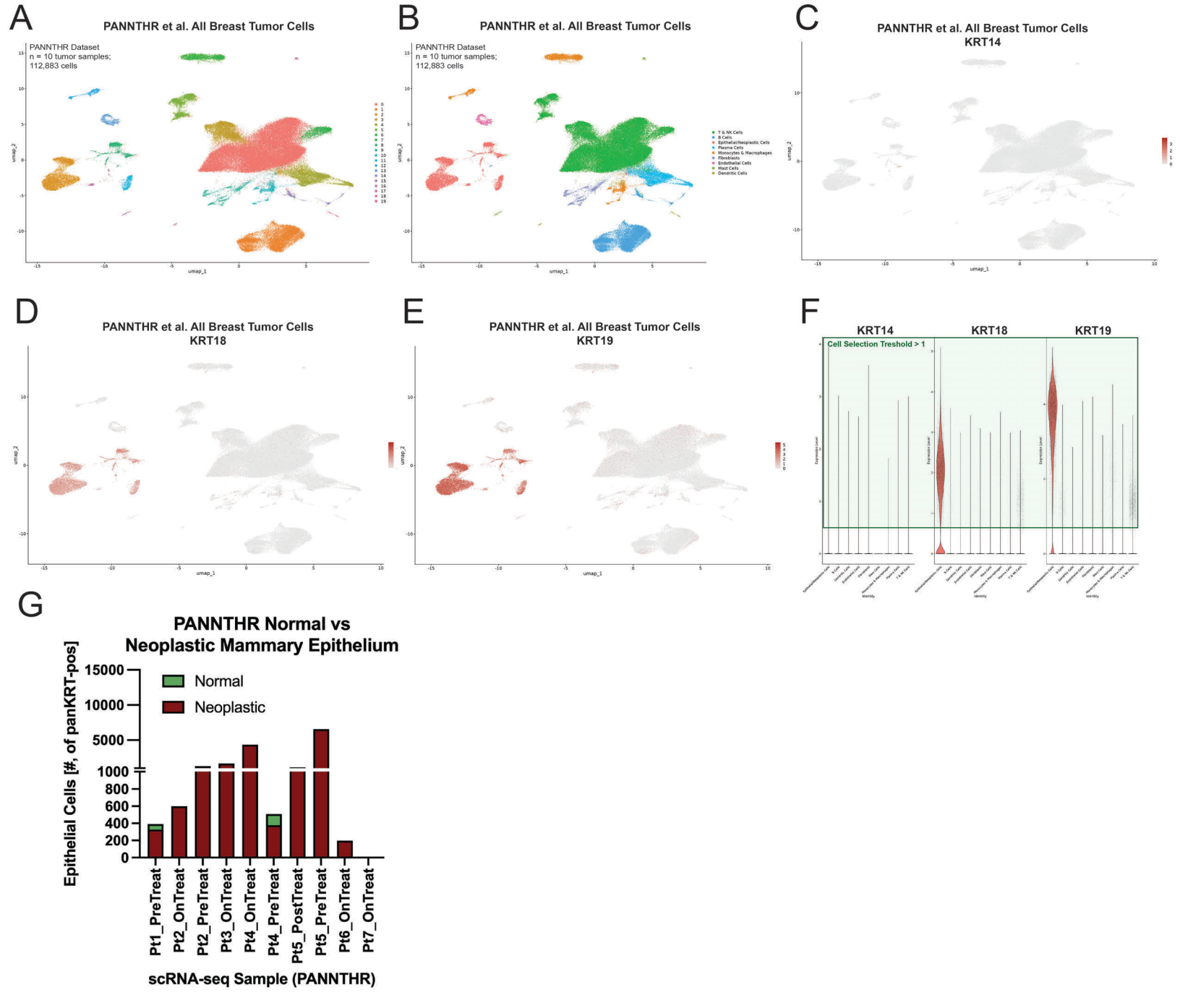

Supplementary Figure 3

Supplementary Figure 3. Collection of cells expressing mammary keratins and identification of neoplastic compartment in the PANNTHR human breast tumor scRNA-seq dataset. (**A**) Umap plot depicting all cells identified in the PANNTHR scRNA-seq dataset and (**B**) their conventional cell type assignments. Cells expressing mammary keratins (**C**) KRT14 (**D**) KRT18 and (**E**) KRT19 are located outside the main epithelial clusters. (**F**) Cells expressing mammary keratins were collected for downstream analysis regardless of cluster location using a threshold gating approach. (**G**) Neoplastic cells with inferred CNVs were refined from the epithelial pool. Normal epithelial cells showed parity with an epithelial reference generated from reduction mammoplasties and were hence omitted from downstream analysis.

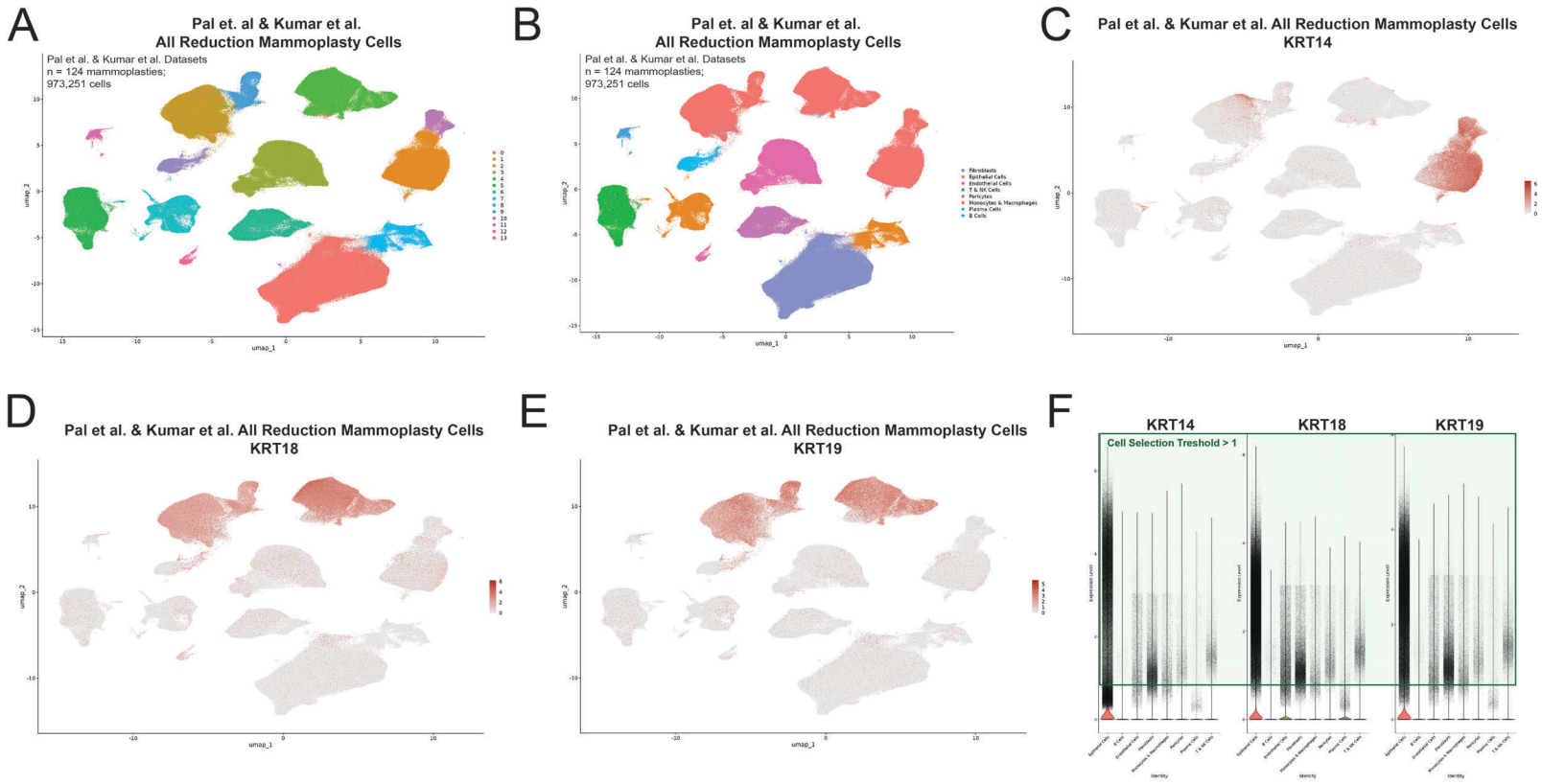

Supplementary Figure 4

Supplementary Figure 4. Collection of cells expressing mammary keratins and identification of mammary epithelial cells in reduction mammoplasties from the Pal *et al.* and Kumar *et al.* scRNA-seq datasets. (**A**) Umap plot depicting all cells identified in the Pal *et al.* and Kumar *et al.* datasets and (**B**) their conventional cell type assignments. Cells expressing mammary keratins (**C**) KRT14 (**D**) KRT18 and (**E**) KRT19 are located outside the main epithelial clusters. (**F**) Cells expressing mammary keratins were collected for downstream analysis regardless of cluster location using a threshold gating approach.

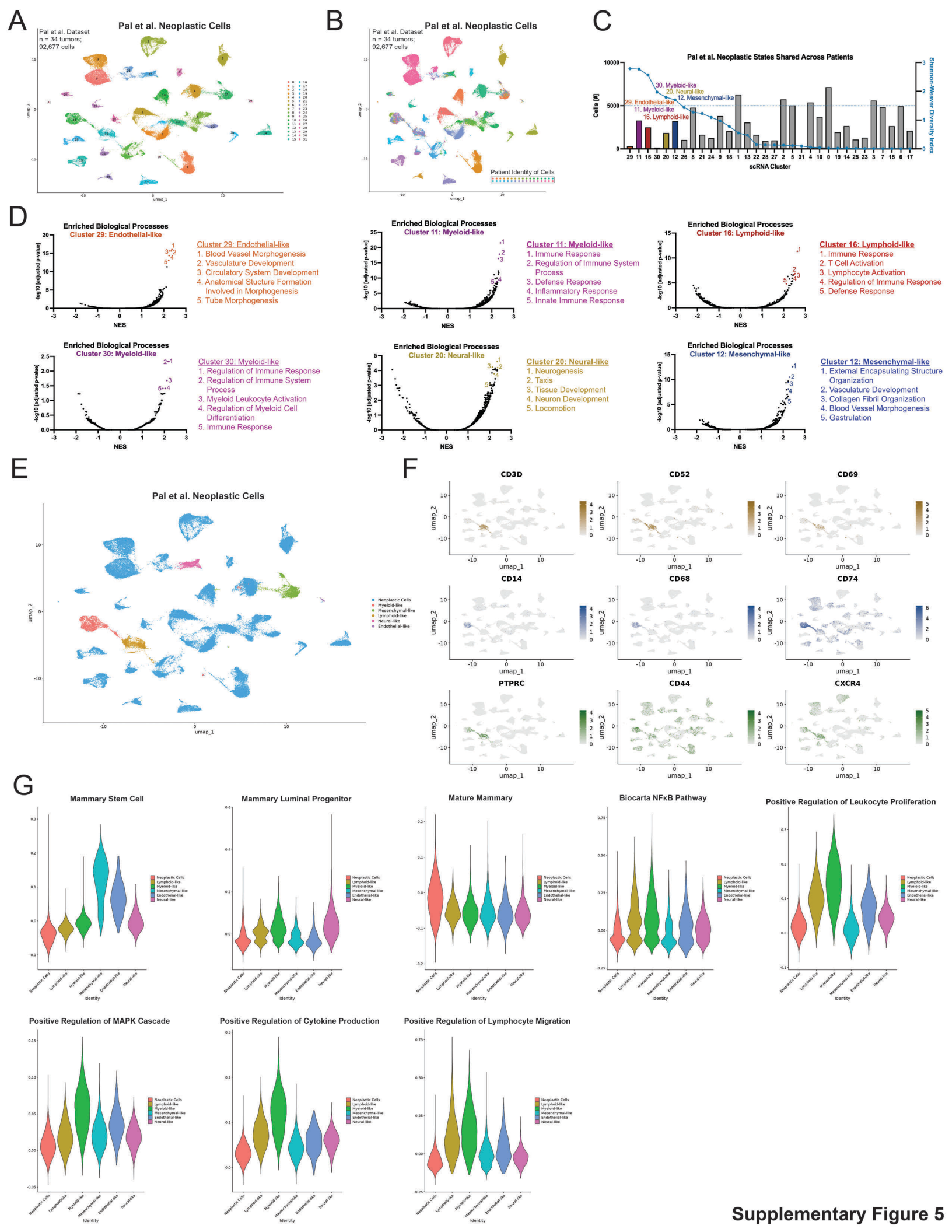

Supplementary Figure 5

Supplementary Figure 5. Extended scRNA-seq analysis of mimicked cell states in the Pal *et al.* human breast tumor scRNA-seq dataset. (**A**) Umap plot depicting neoplastic cells identified in the Pal *et al.* dataset and (**B**) the patient identity of those cells. (**C**) Neoplastic cells in each scRNA-seq cluster, their Shannon-Weaver Diversity Index, and their mimicry designation. (**D**) Mimicry designations are based on enriched Gene Ontology biological processes. (**E**) Umap plot with cluster annotations for mimicked cell states. (**F**) Expression of marker genes polarized toward lymphoid-like cells (gold), myeloid-like cells (blue) as well as both facets of immune mimicry (green). (**G**) The levels of key gene expression signatures for all mimicked cell states across the *Pal et al.* breast tumor dataset.

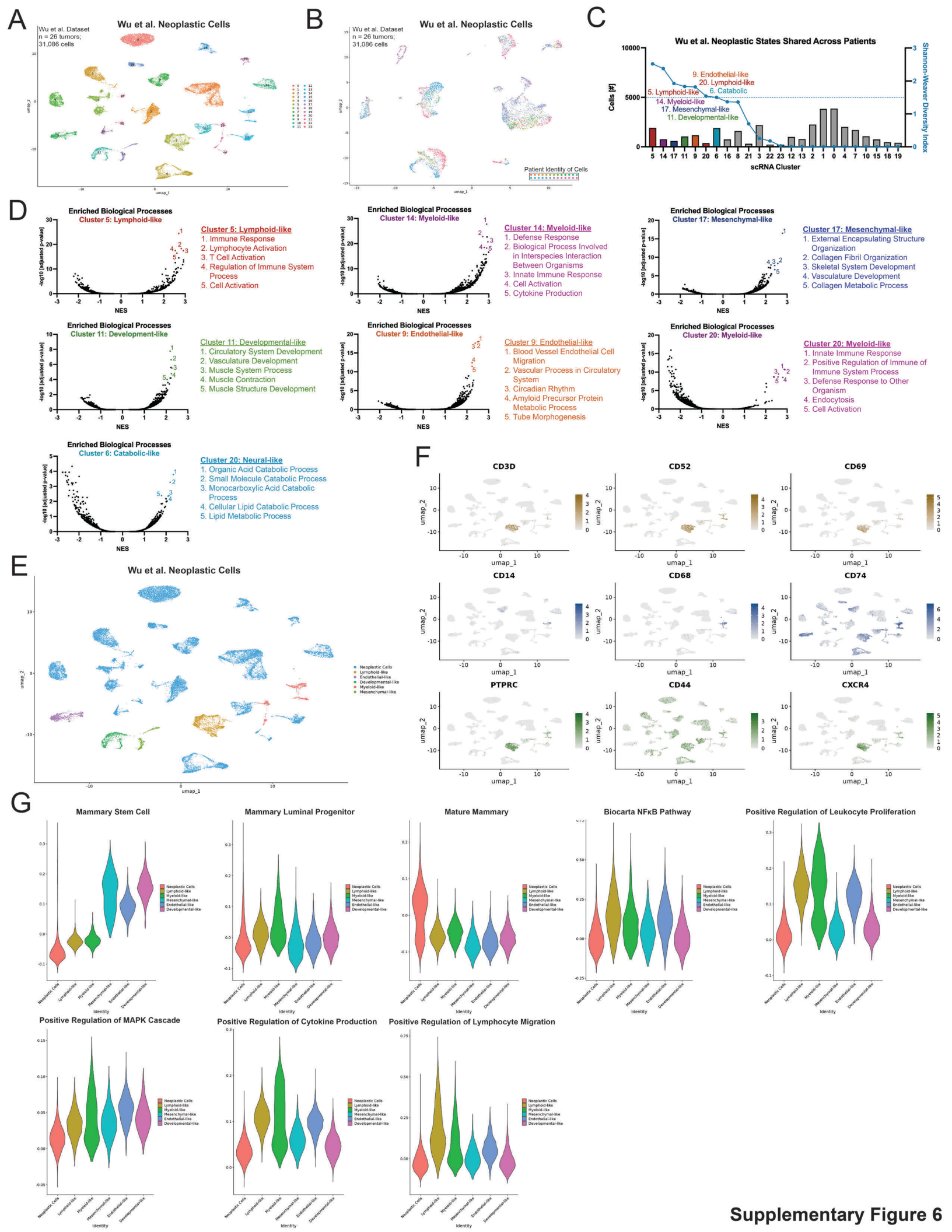

Supplementary Figure 6

Supplementary Figure 6. Extended scRNA-seq analysis of mimicked cell states in the Wu *et al.* human breast tumor scRNA-seq dataset. (**A**) Umap plot depicting neoplastic cells identified in the Wu *et al.* dataset and (**B**) the patient identity of those cells. (**C**) Neoplastic cells in each scRNA-seq cluster, their Shannon-Weaver Diversity Index, and their mimicry designation. (**D**) Mimicry designations are based on enriched Gene Ontology biological processes. (**E**) Umap plot with cluster annotations for mimicked cell states. (**F**) Expression of marker genes polarized toward lymphoid-like cells (gold), myeloid-like cells (blue) as well as both facets of immune mimicry (green). (**G**) The levels of key gene expression signatures for all mimicked cell states across the *Wu et al.* breast tumor dataset.

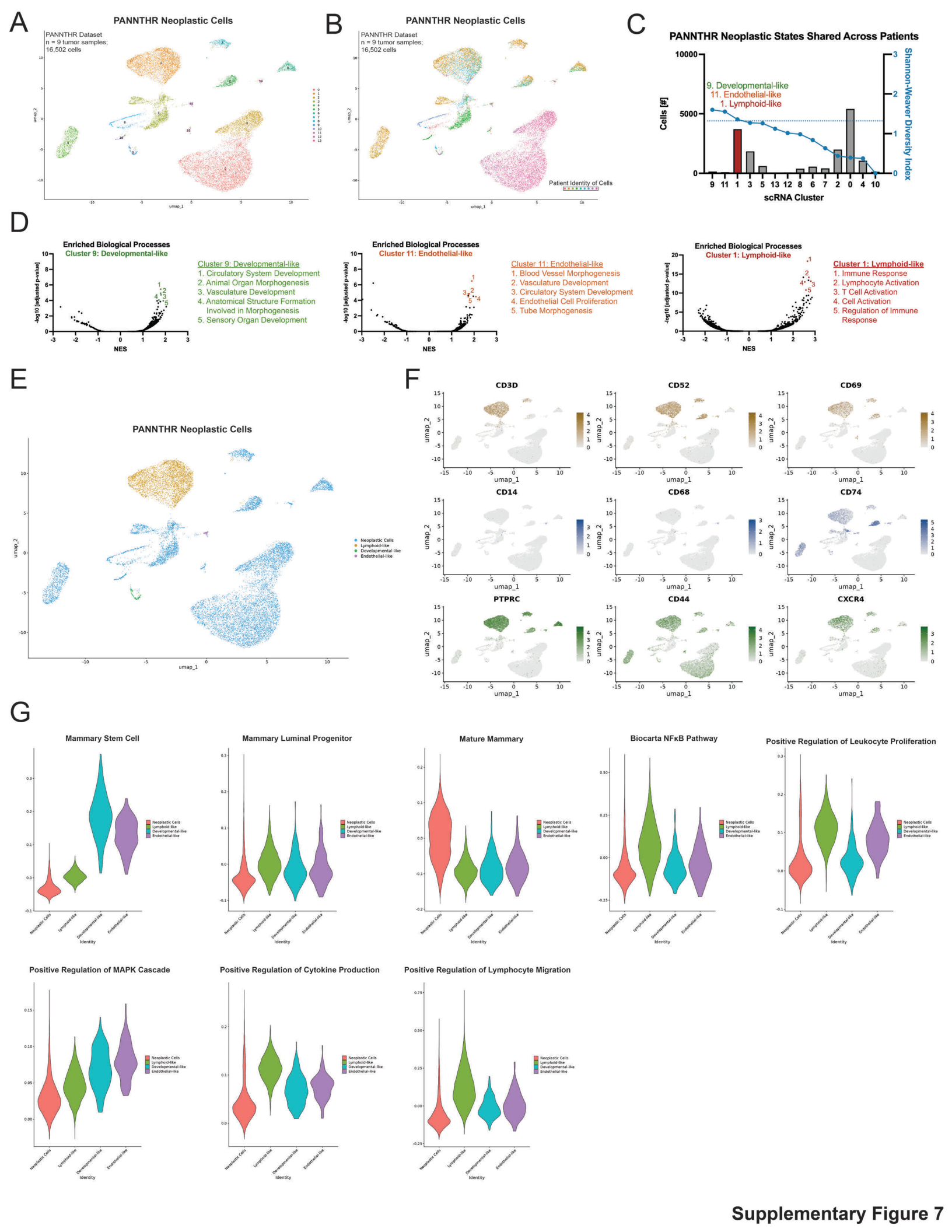

Supplementary Figure 7

Supplementary Figure 7. Extended scRNA-seq analysis of mimicked cell states in the PANNTHR human breast tumor scRNA-seq dataset. (**A**) Umap plot depicting neoplastic cells identified in the PANNTHR dataset and (**B**) the patient identity of those cells. (**C**) Neoplastic cells in each scRNA-seq cluster, their Shannon-Weaver Diversity Index, and their mimicry designation. Shannon-Weaver Diversity Index threshold lowered slightly to allow for collection of immune-mimicked cells. (**D**) Mimicry designations are based on enriched Gene Ontology biological processes. (**E**) Umap plot with cluster annotations for mimicked cell states. (**F**) Expression of marker genes polarized toward lymphoid-like cells (gold), myeloid-like cells (blue) as well as both facets of immune mimicry (green). (**G**) The levels of key gene expression signatures for all mimicked cell states across the PANNTHR breast tumor dataset.

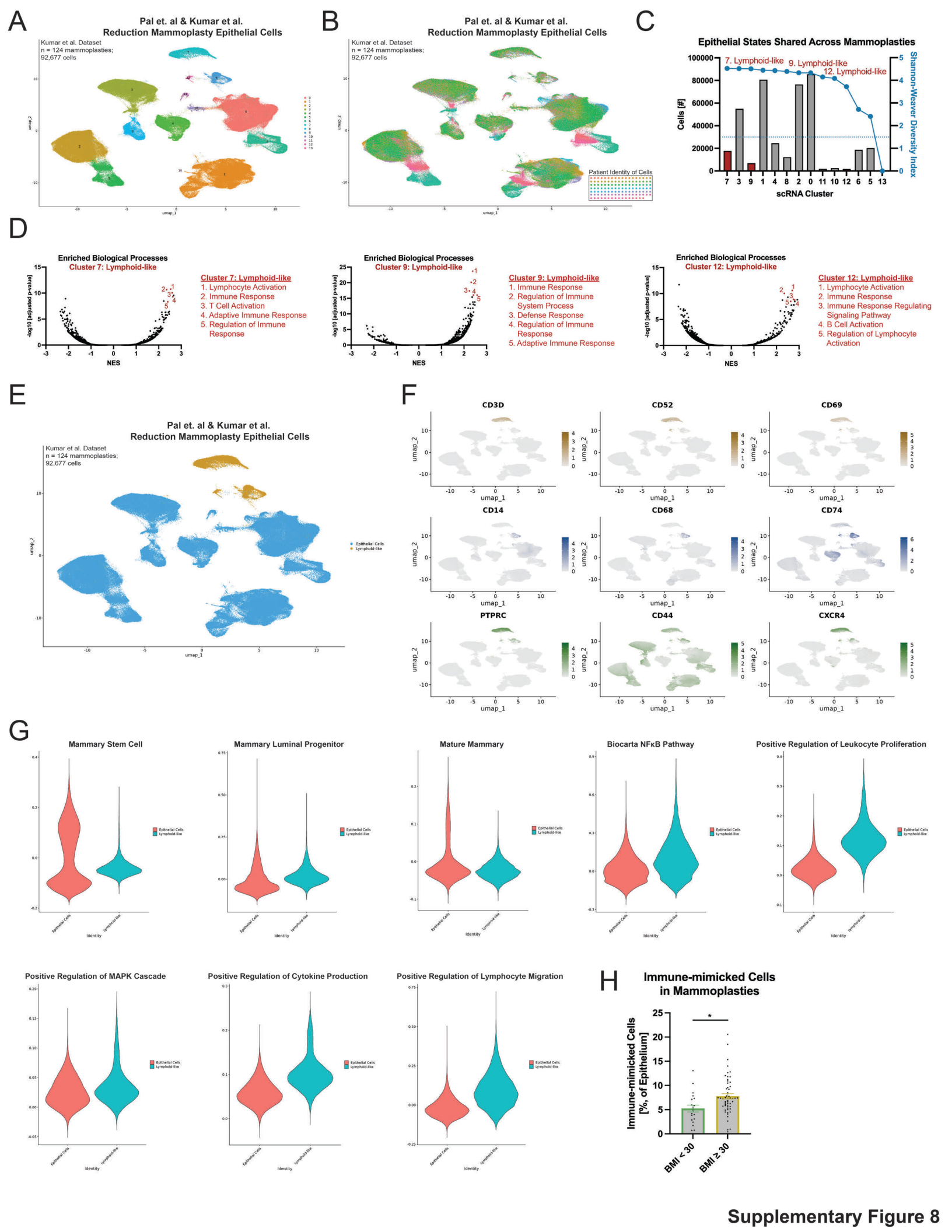

Supplementary Figure 8

Supplementary Figure 8. Extended scRNA-seq analysis of mimicked cell states in reduction mammoplasties from the Pal *et al.* and Kumar *et al.* scRNA-seq datasets. (**A**) Umap plot depicting neoplastic cells identified in the Pal *et al.* and Kumar *et al.* datasets and (**B**) the patient identity of those cells. (**C**) Neoplastic cells in each scRNA-seq cluster, their Shannon-Weaver Diversity Index, and their mimicry designation. (**D**) Mimicry designations are based on enriched Gene Ontology biological processes. (**E**) Umap plot with cluster annotations for mimicked cell states. (**F**) Expression of marker genes polarized toward lymphoid-like cells (gold), myeloid-like cells (blue) as well as both facets of immune mimicry (green). (**G**) The levels of key gene expression signatures for all mimicked cell states across the Pal *et al.* and Kumar *et al.* reduction mammoplasty datasets. (**H**) Immune-mimicked cells are more frequent in reduction mammoplasties from patients with a Body Mass Index (BMI) ≥ 30. * $p < 0.05$; Student's t-test (H).

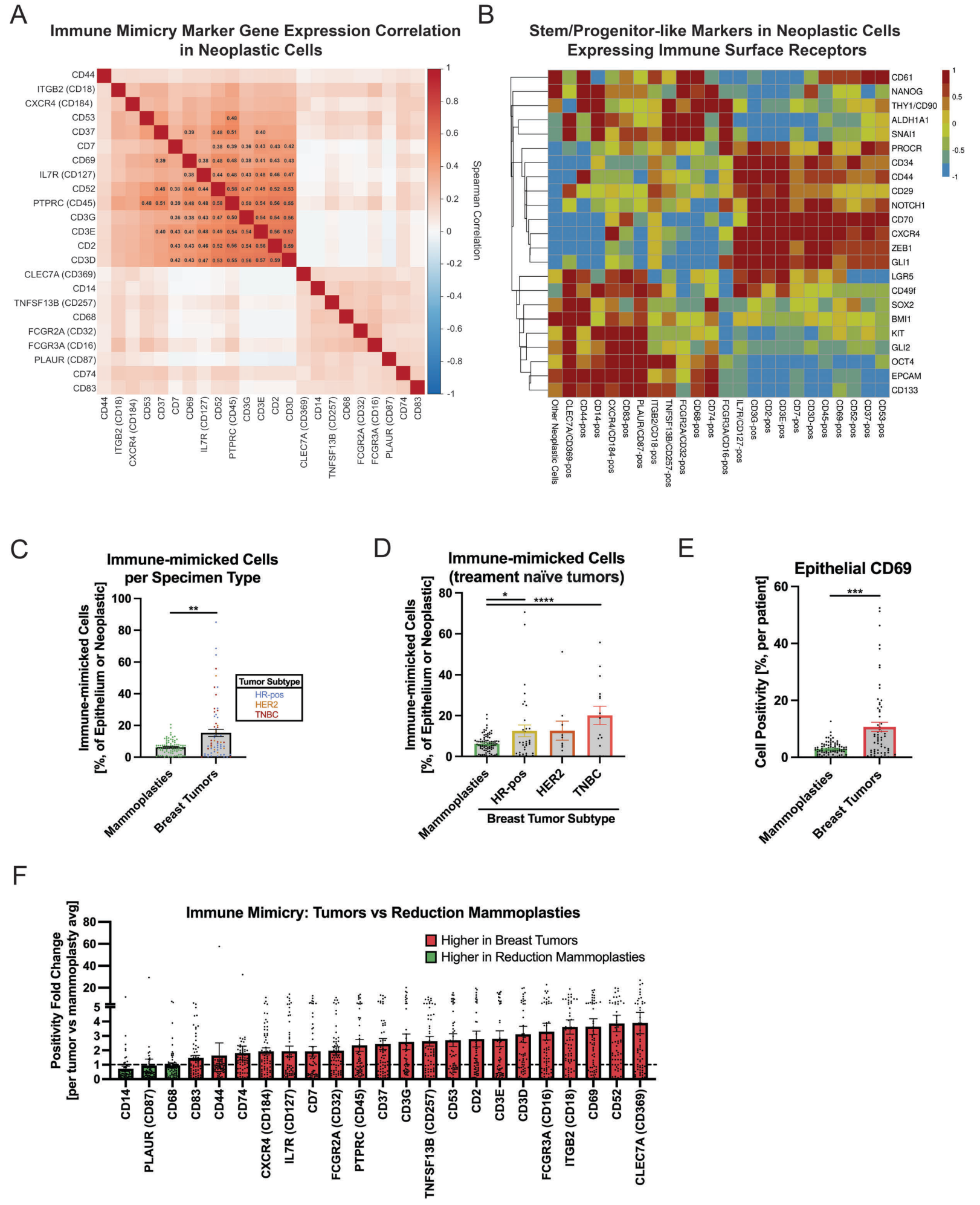

Supplementary Figure 9

Supplementary Figure 9. Additional features of neoplastic immune mimicry identified in scRNA-seq datasets of human breast tumors and reduction mammoplasties. (**A**) Gene expression correlation of immune mimicry surface markers across human breast tumors. Coefficients for significant correlations are indicated. (**B**) Neoplastic expression of leukocyte surface receptor genes accompanies known tumor-initiation markers in breast cancer, with myeloid-like and lymphoid-like receptors being polarized toward different dedifferentiation signatures. (**C**) Neoplastic immune mimicry is elevated in breast tumors versus reduction mammoplasties (**D**) especially those from the triple-negative subtype. (**E**) Comparing the number of cells expressing each immune mimicry receptor in breast tumors versus reduction mammoplasties unveils CD69 to be one of the top markers associated with malignancy. (**F**) The number of neoplastic cells expressing CD69 is significantly elevated in breast tumors compared to reduction mammoplasties. * $p < 0.05$; ** $p < 0.01$; *** $p < 0.001$; **** $p < 0.0001$. Spearman correlation (A), Mann-Whitney test [(C) and (E)], or one-way ANOVA with Tukey correction (D).

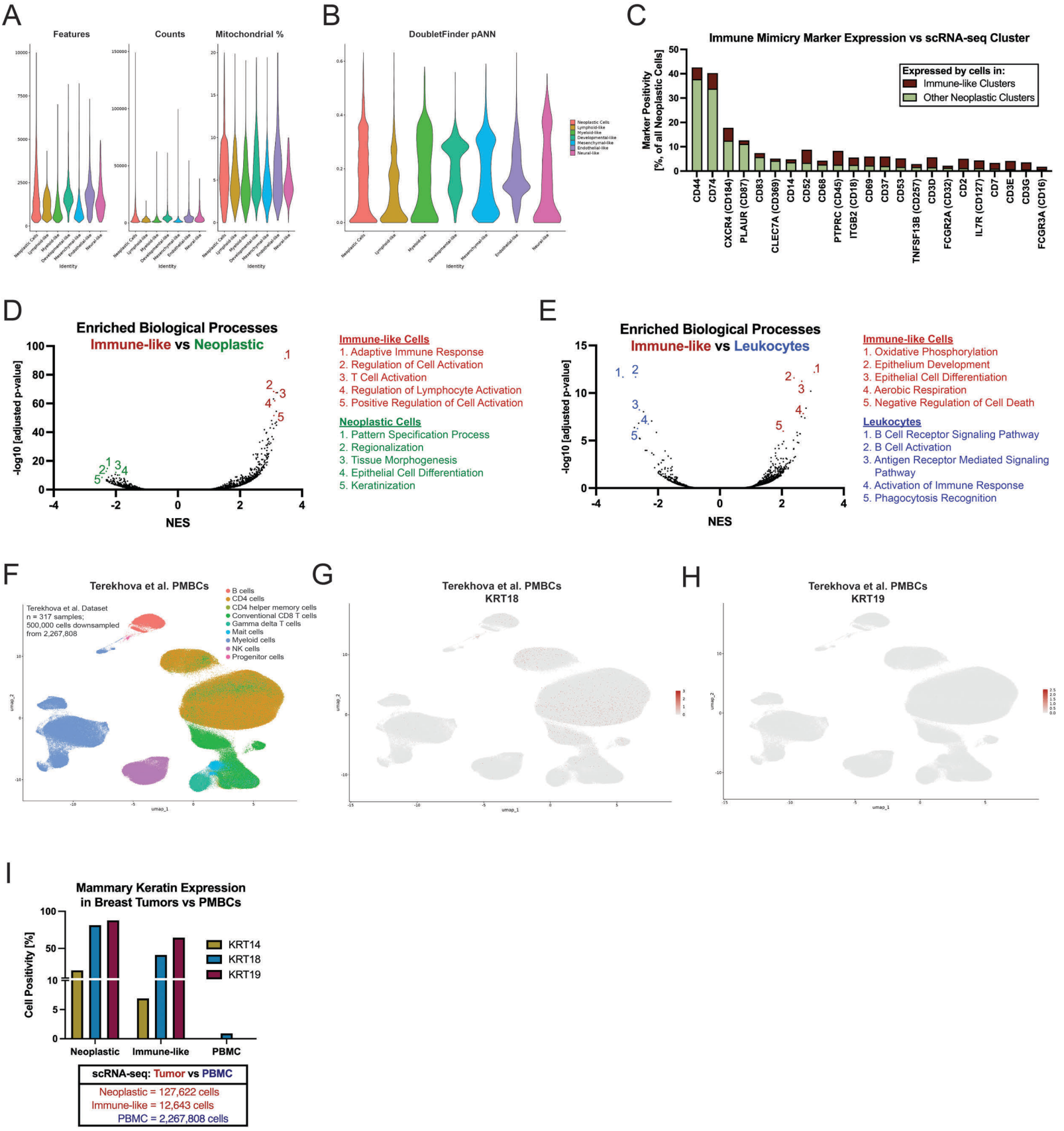

Supplementary Figure 10

Supplementary Figure 10. Computational efforts to ascertain the origin of immune-mimicked cells. (**A**) Assessment of the number of genes (features), molecules (RNA), and percent of mitochondrial reads in various neoplastic cell states found across human breast tumors. For each of these criteria, immune-mimicked cell states mirror that of non-mimicked neoplastic cells. (**B**) The proportion of DoubletFinder's artificial nearest neighbors for immune-mimicked cell states mirrors that of non-mimicked neoplastic cells. (**C**) Cells expressing many leukocyte surface receptors are found in both well-defined epithelial scRNA-seq clusters and immune-like clusters. (**D**) Immune-mimicked cells upregulated leukocyte biological processes when compared with non-mimicked neoplastic cells and (**E**) epithelial/growth processes when compared with tumoral leukocytes. (**F**) Analysis of over 2 million human peripheral blood mononuclear cells reveals (**G**) a tiny fraction expressing KRT18 yet virtually no expression of KRT14 or (**H**) KRT19. Umap shows 500,000 PMBCs downsampled from over 2 million. (**I**) The number of immune-like cells expressing KRT14, KRT18, and KRT19 generally mirrors that of non-mimicked neoplastic cells.

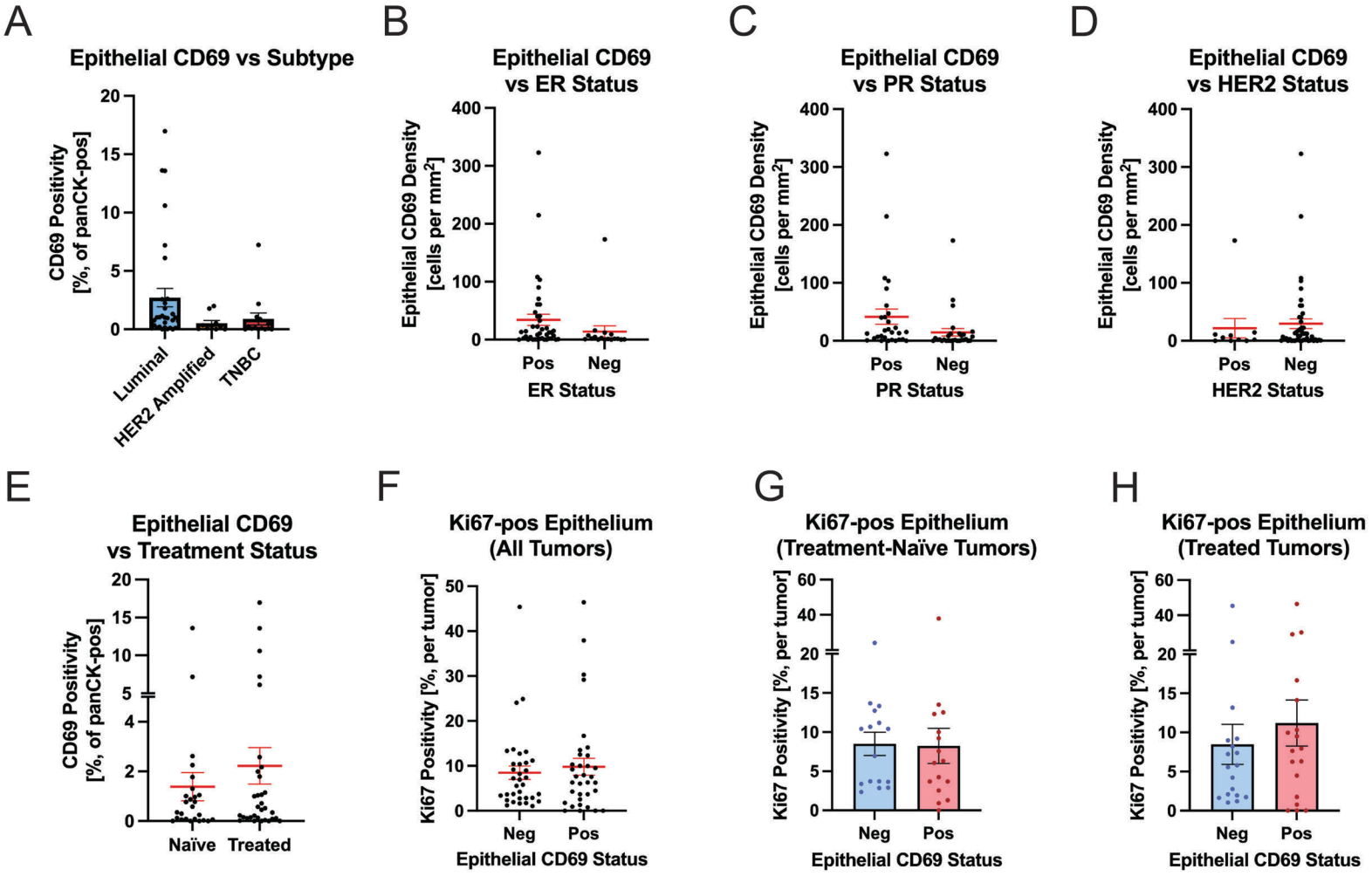

Supplementary Figure 11

Supplementary Figure 11. Histopathologic epithelial CD69 in human breast tumors stratified by clinical parameters. (**A**) The detection of epithelial CD69 in breast tumors according to their subtype. (**B-D**) Epithelial CD69 in individual tumors stratified by breast cancer receptor status such as the (**B**) estrogen receptor, (**C**) progesterone receptor, and (**D**) the HER2 receptor. (**E**) Tumors subjected to therapy before resection may have more epithelia expressing CD69. (**F-H**) Ki67 in CD69-neg versus CD69-pos epithelial cells across (**F**) all breast tumors, (**G**) treatment-naïve breast tumors, and (**H**) treated breast tumors.

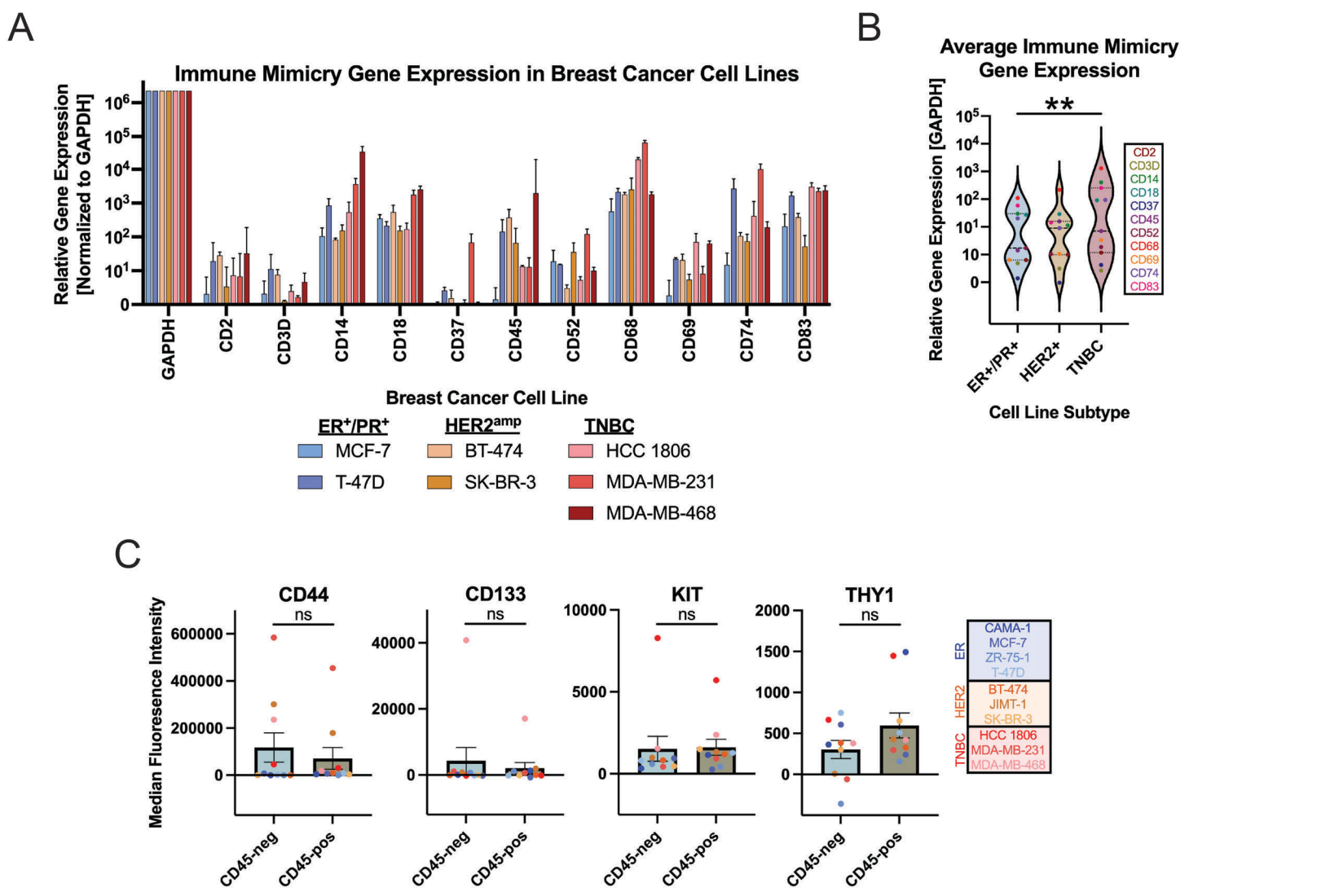

Supplementary Figure 12

Supplementary Figure 12. Continued experimental validation of neoplastic immune mimicry in breast cancer cell lines. (**A**) Evaluation of immune mimicry marker gene expression by qRT-PCR in a subset of breast cancer cell lines. (**B**) Triple-negative breast cancer cell lines express higher average levels of immune mimicry receptors at the RNA level when compared to hormone receptor-positive cell lines. (**C**) CD45-pos immune-mimicked cells do not significantly upregulate standard breast tumor-initiating markers like CD44, CD133, KIT, or THY1, supporting the notion that this is a novel cell state. ns = not significant, ** $p < 0.01$. One-way ANOVA with Dunnett correction (B) or Wilcoxon test (C).

A

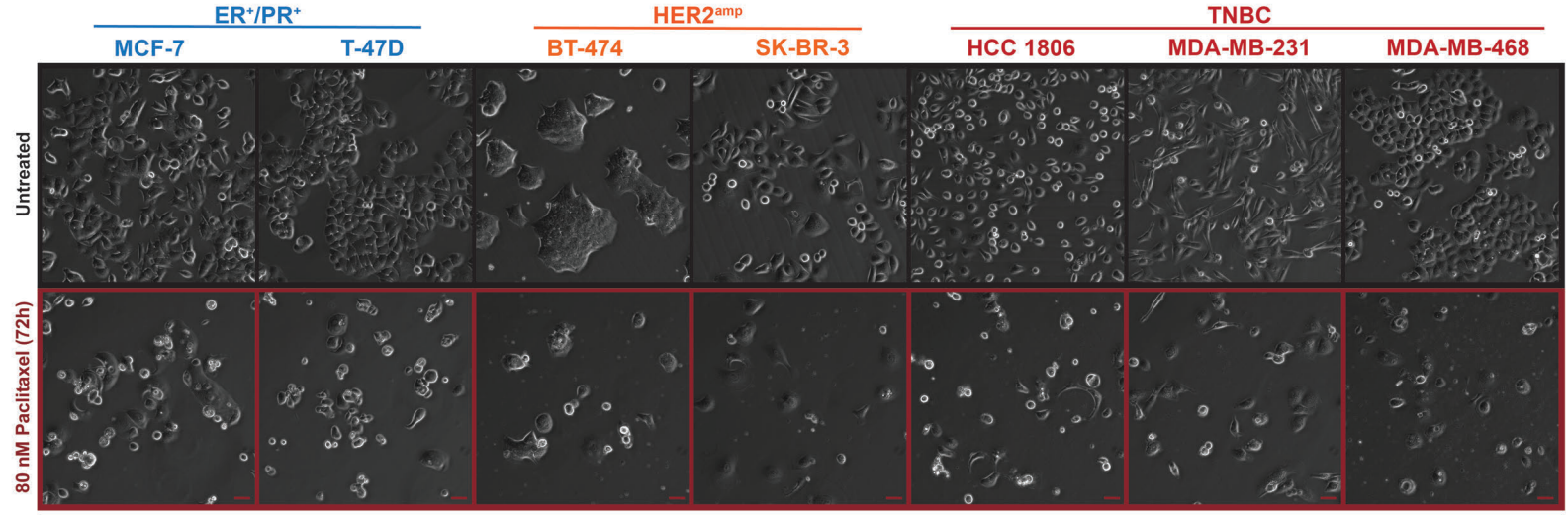

B

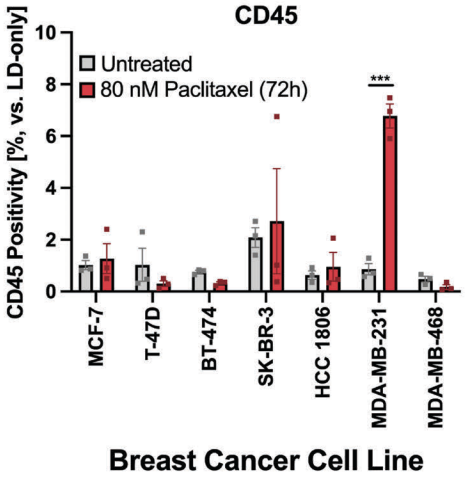

C

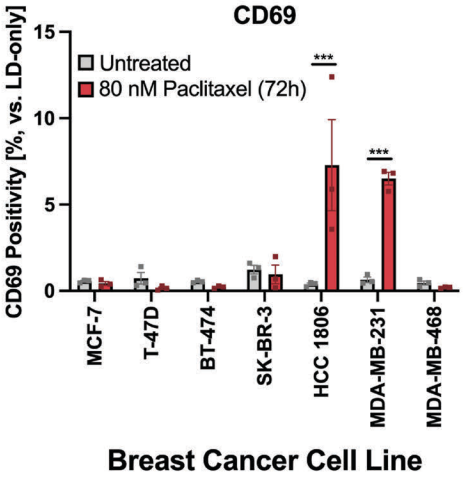

Supplementary Figure 13

Supplementary Figure 13. CD45 and CD69 surface protein after paclitaxel treatment in a subset of breast cancer cell lines. (**A**) Various breast cancer cell lines modeling different disease subtypes were subjected to 80 nM paclitaxel treatment for 72 hours. Surviving cells were subsequently collected for FACS analysis. Scale bar, 25 μm. (**B**) Significant induction of CD45 surface protein in response to paclitaxel was only observed for MDA-MB-231. Flow cytometric analysis represents all stains done in biological triplicate. (**C**) Significant induction of CD69 surface protein after paclitaxel was observed for the triple-negative HCC 1806 and MDA-MB-231 cell lines. Flow cytometric analysis represents all stains performed in biological triplicate. *** $p < 0.001$. Two-way ANOVA with Šidák correction [(B) and (C)].

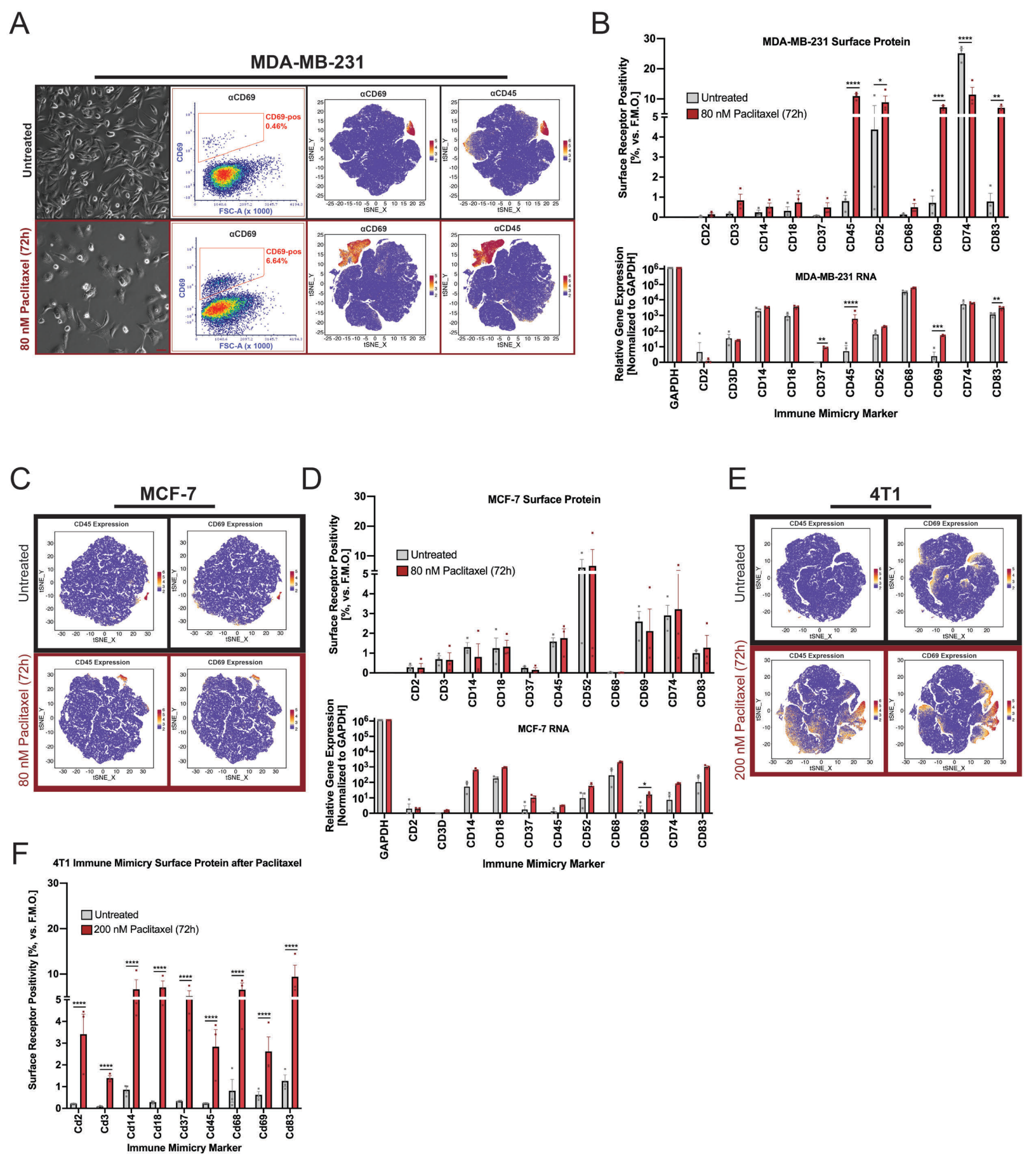

Supplementary Figure 14

Supplementary Figure 14. Paclitaxel treatment elicits immune mimicry in aggressive cell lines. (**A**) For aggressive and metastatic MDA-MB-231 cells, paclitaxel treatment leads to the expansion of an immune-like subpopulation expressing CD45 and CD69. Scale bar, 25 μm. (**B**) The upregulation of leukocyte surface receptors in MDA-MB-231 at the protein level is consistent with increased RNA expression. Flow cytometric analysis represents monostains; biological replicates were performed for both FACS and qRT-PCR. (**C**) For relatively non-metastatic MCF-7 cells, paclitaxel treatment does not expand the immune-like subpopulation expressing CD45 and CD69. (**D**) The lack of immune-mimicry induction in MCF-7 following paclitaxel is witnessed for surface protein as well as RNA. Flow cytometric analysis represents monostains; biological replicates were performed for both FACS and qRT-PCR. (**E-F**) For aggressive and metastatic murine mammary 4T1 cells, paclitaxel treatment leads to the widespread induction of several leukocyte surface receptors. Flow cytometric analysis represents monostains done in biological triplicate. * $p < 0.05$; ** $p < 0.01$; *** $p < 0.001$; **** $p < 0.0001$. Two-way ANOVA with Šidák correction [(B), (D) and (F)].

A

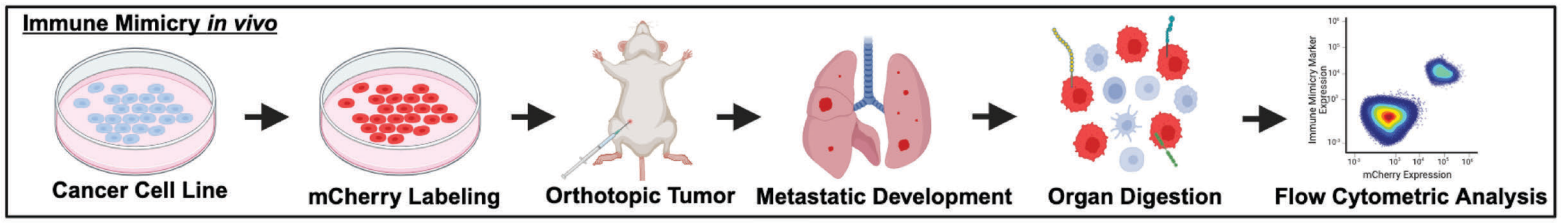

B

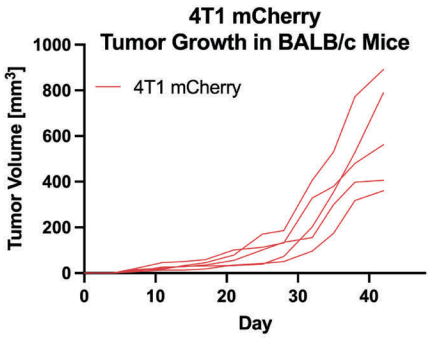

C

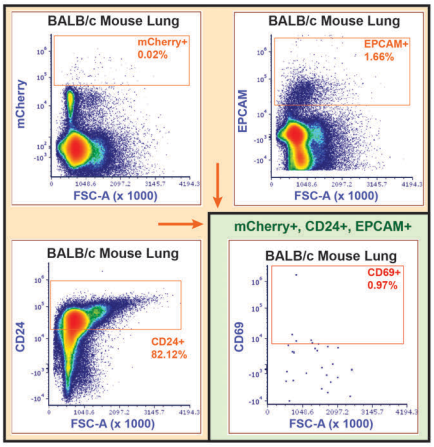

D

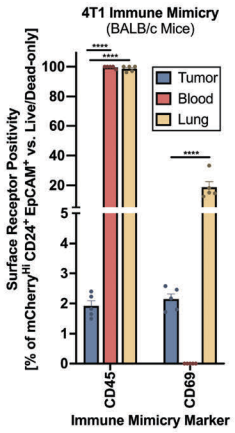

E

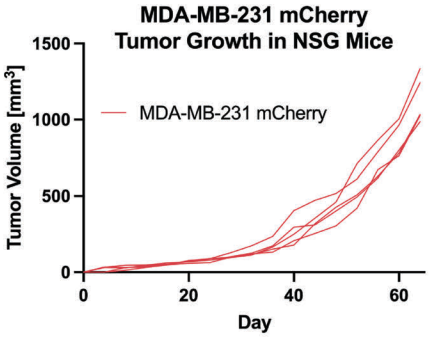

F

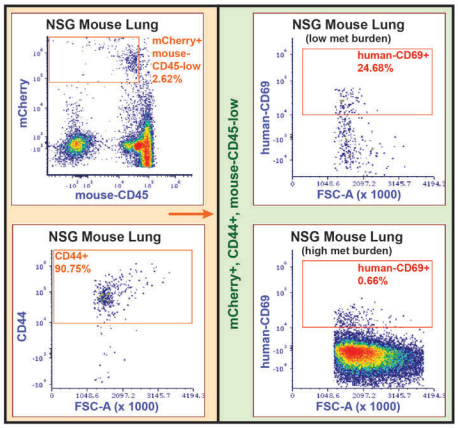

G

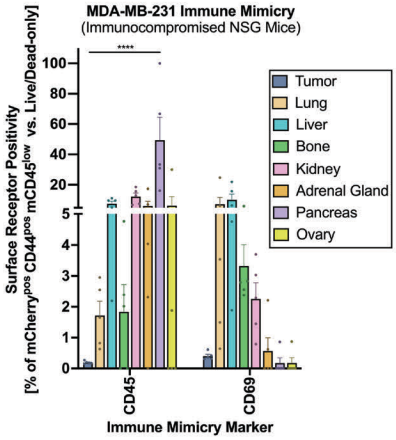

H

MDA-MB-231 CD69 Positivity in NSG Lung Metastases

Mouse	Total MDA-MB-231	CD69-pos MDA-MB-231
Lung #1	0.08%	24.68%
Lung #2	0.09%	6.30%
Lung #3	0.23%	3.54%
Lung #4	0.45%	1.49%
Lung #5	2.45%	0.66%

Spearman Correlation: -1.00
p = 0.0167

Supplementary Figure 15

Supplementary Figure 15. CD45 and CD69 are induced during 4T1 and MDA-MB-231 metastasis in mice. (**A**) 4T1 and MDA-MB-231 cells were transduced with mCherry to facilitate sorting from metastatic tissues after orthotopic tumor growth in mice. (**B**) Tumor growth curves for 4T1 cells expressing mCherry after injection into BALB/c mice. (**C**) At endpoint, the tumor, blood, and lungs of mice were digested and the prospective flow cytometric analysis of 4T1 cells leveraged three redundant epithelial makers: mCherry, CD24, and EpCAM. (**D**) Metastatic 4T1 cells expressing mCherry, CD24, and EpCAM showed upregulation of CD45 in both the blood and lungs whereas CD69 was only upregulated in the lung. (**E**) Tumor growth curves for MDA-MB-231 cells expressing mCherry after injection into immunocompromised NSG mice. (**F**) Prospective identification of MDA-MB-231 cells from mouse tissue leveraged mCherry and CD44, which are two markers ubiquitously expressed in the cell line. These cells were also found to have lower levels of mouse-CD45 though amid suspicion that antibodies targeting mouse CD45 may have cross-reacted with the human epitope and vice versa. Examples of human CD69 staining in lungs with low versus high metastatic burden shown. (**G**) MDA-MB-231 cells ostensibly positive for CD45 and CD69 were retrieved from various metastatic tissues in immunocompromised NSG mice with (**H**) CD69 positivity being inversely correlated with lung metastatic burden. Antibodies used in this experiment targeted human CD45 and CD69 epitopes on MDA-MB-231 cells within dissociated mouse tissue. **** $p < 0.0001$. Two-way ANOVA with Šidák correction [(D) and (G)] or Spearman correlation (H).

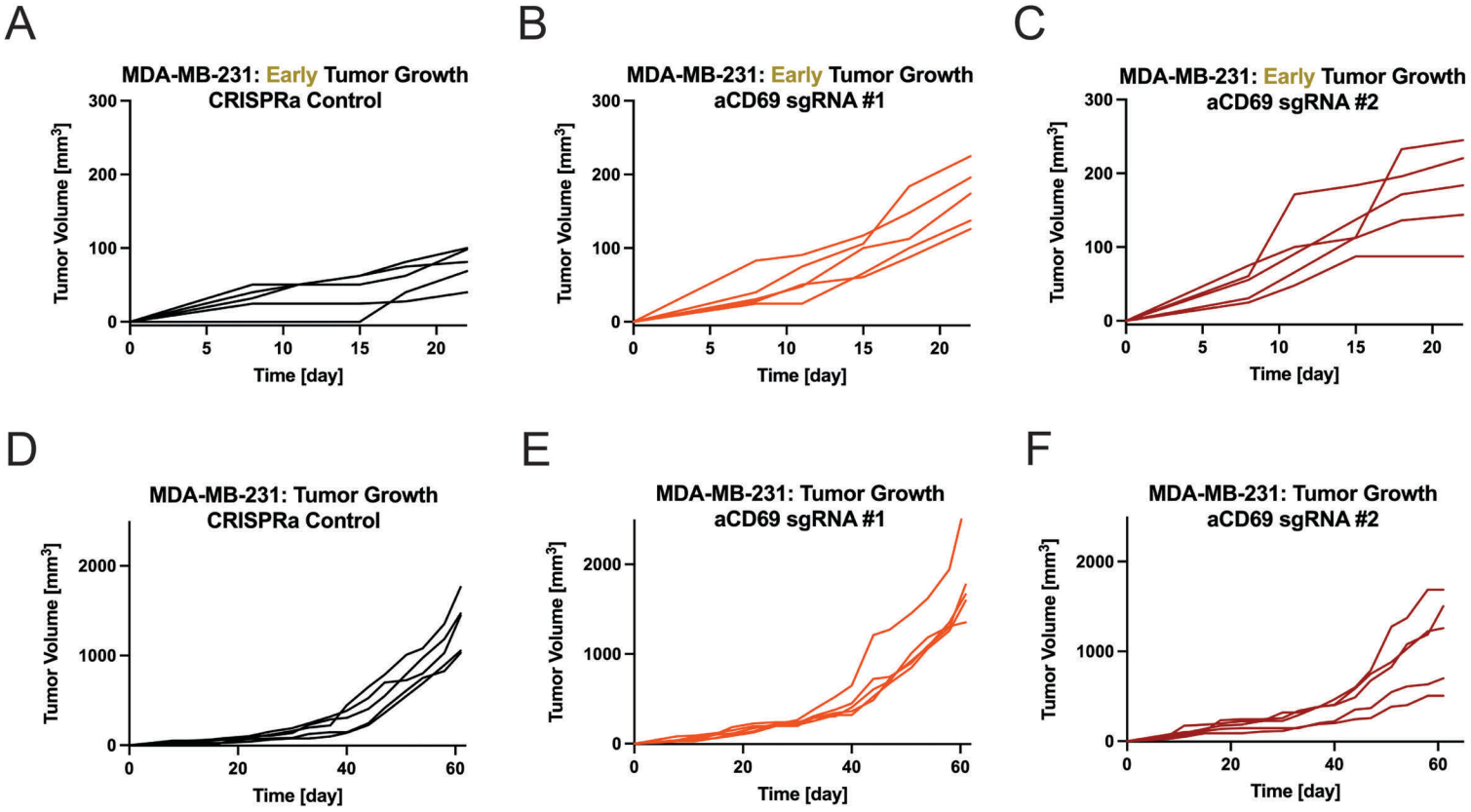

Supplementary Figure 16

Supplementary Figure 16. Extended data for MDA-MB-231 CD69 CRISPR-activation experiments and the disruption of CD69 using CRISPR/Cas9. (**A-F**) Spider plots showing the (**A-C**) early and (**D-F**) entire growth of individual tumors following the CRISPR-activation of CD69.

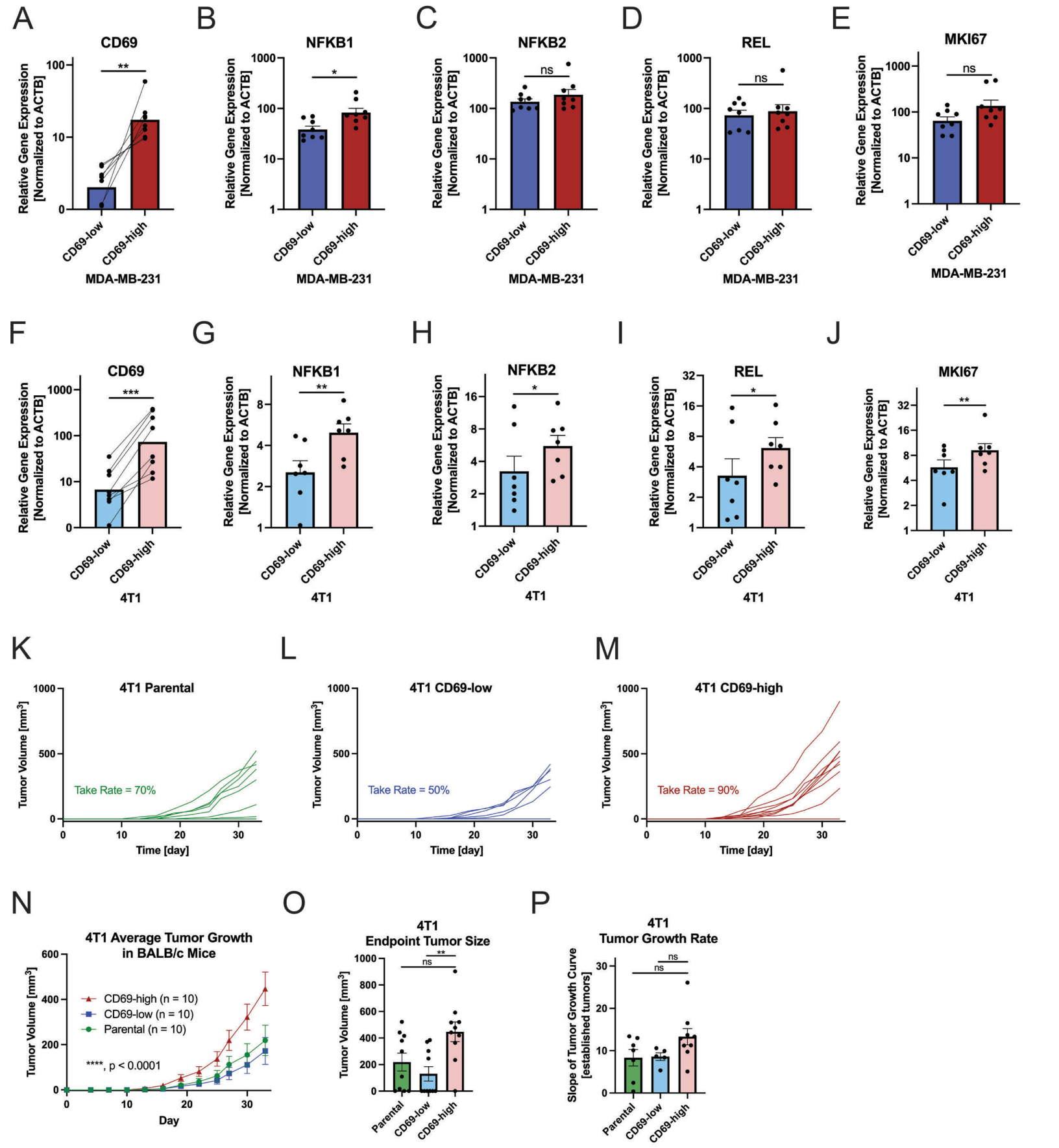

Supplementary Figure 17

Supplementary Figure 17. Extended data for MDA-MB-231 and 4T1 CD69 magnetic sorting experiments. (**A**-**E**) RNA expression of (**A**) CD69, (**B**-**D**) NFκB genes, and (**E**) MKI67 in sorted MDA-MB-231 cells. (**F**-**J**) RNA expression of (**F**) CD69, (**G**-**I**) NFκB genes, and (**J**) MKI67 in sorted 4T1 cells. (**K**-**M**) Spider plots exhibiting the growth of individual 4T1 tumors derived from the parental control versus CD69-low and CD69-high sorted subpopulations. (**N**) The outcome of this study summarized by (**N**) tumor growth, (**O**) endpoint tumor size, and (**P**) the growth rate of established tumors. ns = not significant, * $p < 0.05$; ** $p < 0.01$; *** $p < 0.001$; **** $p < 0.0001$. Student's t-test [(A), (B), (C), (D), (E), (F), (G), (H), (I) and (J)], two-way ANOVA, or one-way ANOVA with Tukey correction [(O) and (P)].

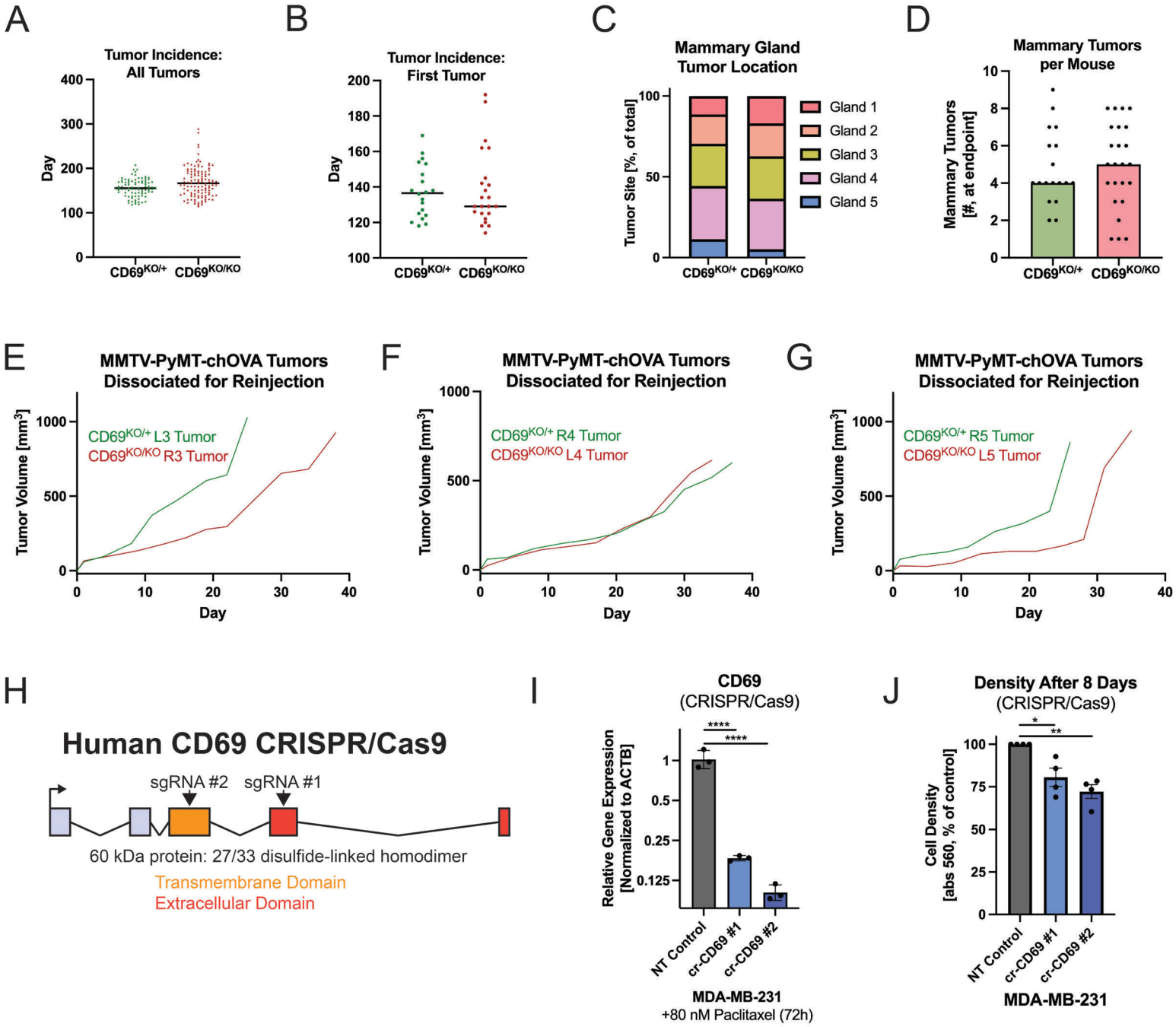

Supplementary Figure 18

Supplementary Figure 18. Extended data for MMTV-PyMT-CD69$^{KO/KO}$ experiments. (**A**-**C**) There is no statistical difference in the detection time of spontaneous tumors for the (**A**) first tumor or (**B**) all tumors in MMTV-PyMT-CD69$^{KO/+}$ and MMTV-PyMT-CD69$^{KO/KO}$ mice. (**C**) The distribution of mammary tumors and (**D**) the number developed in MMTV-PyMT-CD69$^{KO/+}$ and MMTV-PyMT-CD69$^{KO/KO}$ mice is similar. (**E**-**G**) Tumors attaining similar endpoint sizes were dissociated for reinjection back into CD69$^{KO/+}$ mice. (**H**) CD69 CRISPR/Cas9 sgRNAs targeting the protein's extracellular or transmembrane domain were transduced into MDA-MB-231 along with constitutively active Cas9. (**I**) MDA-MB-231 cells with disrupted CD69 have reduced RNA expression following paclitaxel treatment, which was done to compare CD69 induction capacity. (**J**) MDA-MB-231 cells harboring disrupted CD69 achieve lower density following growth *in vitro*. * $p < 0.05$; ** $p < 0.01$; **** $p < 0.0001$. One-way ANOVA with Tukey correction [(I) and (J)].

Table S1. Reagents used for multiplexed immunohistochemistry staining.

Staining Order	Marker	Antibody Clone	Vendor	Catalog #
1	Hematoxylin & Eosin		Hematoxylin: Vector, Eosin: Fisher	Hematoxylin: H-3401-500, Eosin: 22-110-637
2	CD69	Polyclonal	Sigma	HPA050525
3	CD45	H130	Fisher	50-126-09
4	CD3	SP7	Fisher	RM9107S
5	CD20	L26	Abcam	ab9475
6	CD68	PG-M1	Abcam	ab783
7	Vimentin	280618	R&D Systems	MAB2105
8	CD11b	EPR1344	Abcam	ab133357
9	CD163	10D6	ThermoFisher Scientific	MA5-11458
10	CD31	Polyclonal	Abcam	Ab28364
11	CD8	C8/144B	Fisher	PIMA513473
12	KRT19	Polyclonal	Sigma	HPA002465
13	PanCK	AE1/AE3//5D3	Abcam	ab86734
14	KI67	SP6	Sigma	275R-17
15	H3/NUCA	H3: D1H2, NucA: NM106	H3: Cell Signalling Technologies, NucA: Abcam	H3: 4999L NucA: ab215396
16	Hematoxylin		Vector	H-3401-500

Table S2. Human antibodies used for flow cytometric analyses.

Marker	Antibody Clone	Fluorophore	Company	Catalog
CD2	TS1/8	PE/Cy5	Biolegend	300209
CD3	SK7	BV 750	Biolegend	344845
CD14	M5E2	BV 711	Biolegend	301837
CD18	TS1/18	PE/Dazzle 594	Biolegend	302127
CD24	ML5	PerCP	Biolegend	311113
CD37	M-B371	FITC	Biolegend	356303
CD44	IM7	Pac Blue	Biolegend	103020
CD45	HI30	AF 700	Biolegend	304023
CD52	HL186	PerCP/Cy5.5	Biolegend	316009
CD68	Y1/82A	BV 785	Biolegend	333825
CD69	FN50	PE/Cy7	Biolegend	310912
CD74	LN2	PE	Biolegend	326807
CD83	HB15e	APC/Fire 750	Biolegend	305331
CD133	S16015F	BV 421	Biolegend	393907
KIT (CD117)	104D2	BV 605	Biolegend	313217
THY1 (CD90)	5E10	BV 650	Biolegend	328143
Ki67	Ki-67	Pac Blue	Biolegend	350511
Live/Dead		Zombie NIR	Biolegend	423106
CD69	FN50	APC	Biolegend	985206
Live/Dead		Zombie Violet	Biolegend	423114

Table S3. Murine antibodies used for flow cytometric analyses.

Marker	Antibody Clone	Fluorophore	Company	Catalog
CD2	RM2-5	PerCP/Cy5.5	Biolegend	100115
CD3	17A2	BV 750	Biolegend	100249
CD14	Sa14-2	APC/Fire 750	Biolegend	123331
CD18	M18/2	FITC	Biolegend	101405
CD24	M1/69	AF 700	Biolegend	101835
CD37	Duno85	PE	Biolegend	146203
CD44	IM7	Pac Blue	Biolegend	103020
CD45	30-F11	BV 650	Biolegend	103151
CD68	FA-11	BV 711	Biolegend	137029
CD69	H1.2F3	APC	Biolegend	104514
CD83	Michel-19	PE/Cy7	Biolegend	121517
CD133	315-2C11	BV 421	Biolegend	141213
EpCAM (CD326)	G8.8	BV 510	Biolegend	118231
KIT (CD117)	AKC2	BV 785	Biolegend	135138
THY1 (CD90)	30-H12	PE/Cy5	Biolegend	105314
Ki67	B56	BV 480	BD Biosciences	566109
CD45	30-F11	PerCP	Biolegend	103130
Live/dead		Zombie NIR	Biolegend	423106

Table S4. qRT-PCR primers used in this study.

Primer	Species	Sequence
hACTB_FWD	Human	CATGTACGTTGCTATCCAGGC
hACTB_REV	Human	CTCCTTAATGTCACGCACGAT
hGAPDH_met_FWD	Human	TCAAGGCTGAGAACGGGAAG
hGAPDH_met_REV	Human	CGCCCCACTTGATTTTGGAG
hCD2_FWD	Human	TCAAGAGAGGGTCTCAAAACCA
hCD2_REV	Human	CCATTCATTACCTCACAGGTCAG
hCD3D_FWD	Human	ACTGGCTACCCTTCTCTCG
hCD3D_REV	Human	CCGTTCCCTCTACCCATGTGA
hCD14_FWD	Human	ACGCCAGAACCTTGTGAGC
hCD14_REV	Human	GCATGGATCTCCACCTCTACTG
hCD18_FWD	Human	TGCGTCCTCTCTCAGGAGTG
hCD18_REV	Human	GGTCCATGATGTCGTCAGCC
hCD37_FWD	Human	GCTGGGACTATGTGCAGTTCC
hCD37_REV	Human	ACCCGTTACCTCTCAGGATGA
hCD45_FWD	Human	ACCACAAGTTTACTAACGCAAGT
hCD45_REV	Human	TTTGAGGGGGATTCCAGGTAAT
hCD52_FWD	Human	TCTTCCTCCTACTCACCATCAG
hCD52_REV	Human	CCTCCGCTTATGTTGCTGGA
hCD68_FWD	Human	TGGGGCAGAGCTTCAGTTG
hCD68_REV	Human	TGGGGCAGGAGAAACTTTGC
hCD69_FWD	Human	ATTGTCCAGGCCAATACACATT
hCD69_REV	Human	CCTCTCTACCTGCGTATCGTTTT
hCD74_FWD	Human	GACGAGAACGGCAACTATCTG
hCD74_REV	Human	GTTGGGGAAGACACACCAGC
hCD83_FWD	Human	AAGGGGCAAAATGGTTCTTTCG
hCD83_REV	Human	GCACCTGTATGTCCCCGAG
hCD69_upstream_FWD	Human	GTAGCTTGACTTGACCTGAGATT
hCD69_upstream_REV	Human	ATGGTGATGAAGACCACATTCA
hNFKB1_FWD	Human	AACAGAGAGGATTTCGTTTCCG
hNFKB1_REV	Human	TTTGACCTGAGGGTAAGACTTCT
hNFKB2_FWD	Human	ATGGAGAGTTGCTACAACCCA
hNFKB2_REV	Human	CTGTTCCACGATCACCAGGTA
hREL_FWD	Human	GCAGAGGGGAATGCGTTTTAG
hREL_REV	Human	AGAAGGGTATGTTCGGTTGTTG
hMKI67_FWD	Human	GCCTGCTCGACCCTACAGA
hMKI67_REV	Human	GCTTGTCAACTGCGGTTGC
mActb_FWD	Mouse	GGCTGTATTCCCCTCCATCG
mActb_REV	Mouse	CCAGTTGGTAACAATGCCATGT
mGapdh_FWD	Mouse	AGGTCGGTGTGAACGGATTTG
mGapdh_REV	Mouse	TGTAGACCATGTAGTTGAGGTCA
mCd69_FWD	Mouse	CCCTTGGGCTGTGTTAATAGTG
mCd69_REV	Mouse	AACTTCTCGTACAAGCCTGGG
mCd45_FWD	Mouse	GTTTTCGCTACATGACTGCACA

mCd45_REV	Mouse	AGGTTGTCCAACTGACATCTTTC
mNfkb1_Fwd	Mouse	ATGGCAGACGATGATCCCTAC
mNfkb1_Rev	Mouse	TGTTGACAGTGGTATTTCTGGTG
mNfkb2_Fwd	Mouse	GGCCGGAAGACCTATCCTACT
mNfkb2_Rev	Mouse	CTACAGACACAGCGCACACT
mRel_Fwd	Mouse	AGAGGGGAATGCGGTTTAGAT
mRel_Rev	Mouse	TTCTGGTCCAAATTCTGCTTCAT
mMki67_Fwd	Mouse	ATCATTGACCGCTCCTTTAGGT
mMki67_Rev	Mouse	GCTCGCCTTGATGGTTCCT

Table S5. Oligos used for cloning CRISPR-a and CRISPR/Cas9 plasmids.

sgRNA Oligo	Sequence
hCD69_CRISPRa_sg1_top	CACCGTGTGTTGTTGTGGTGAAGTA
hCD69_CRISPRa_sg1_bottom	AAACTACTTCACCACAACAACACAC
hCD69_CRISPRa_sg2_top	CACCGCTATACATTGTCTGGTCCAC
hCD69_CRISPRa_sg2_bottom	AAACGTGGACCAGACAATGTATAGC
hCD69_CRISPRcas9_sg1_top	CACCGAACTTTCTAAAACGATACGC
hCD69_CRISPRcas9_sg1_bottom	AAACGCGTATCGTTTTAGAAAGTTC
hCD69_CRISPRcas9_sg2_top	CACCGGTGGGCCAATACAATTGTCC
hCD69_CRISPRcas9_sg2_bottom	AAACGGACAATTGTATTGGCCCACC